Computational study of CO2 methanation on Ru/CeO2 model surfaces

ACS Catalysis

pubs.acs.org/acscatalysis
Research Article

Computational Study of CO_2 Methanation on Ru/CeO_2 Model Surfaces: On the Impact of Ru Doping in CeO_2

Lulu Chen, Ivo A. W. Filot, and Emiel J. M. Hensen*

Cite This: ACS Catal. 2023, 13, 15230−15247
Read Online

ACCESS | Metrics & More | Article Recommendations | Supporting Information

ABSTRACT: The Sabatier reaction ($CO_2 + H_2 \rightarrow CH_4 + H_2O$) can contribute to renewable energy storage by converting green H_2 with waste CO_2 into CH_4. Highly dispersed Ru on CeO_2 represents an active catalyst for the CO_2 methanation. Here, we investigated the support effect by considering a single atom of Ru and a small Ru cluster on CeO_2 (Ru_6/CeO_2). The influence of doping CeO_2 with Ru was investigated as well ($Ru_6/RuCe_{x-1}O_{2x-1}$). Density functional theory was used to compute the reaction energy diagrams. A single Ru atom on CeO_2 can only break one of the C−O bonds in adsorbed CO_2, making it only active in the reverse water−gas shift reaction. In contrast, Ru_6 clusters on stoichiometric and Ru-doped CeO_2 are active methanation catalysts. CO is the main reaction intermediate formed via a COOH surface intermediate. Compared to an extended Ru(11−21) surface containing step-edge sites where direct C−O bond dissociation is facile, C−O dissociation proceeds via H-assisted pathways (CO → HCO → CH) on Ru_6/CeO_2 and $Ru_6/RuCe_{x-1}O_{2x-1}$. A higher CO_2 methanation rate is predicted for $Ru_6/RuCe_{x-1}O_{2x-1}$. Electronic structure analysis clarifies that the lower activation energy for HCO dissociation on $Ru_6/RuCe_{x-1}O_{2x-1}$ is caused by stronger electron−electron repulsion due to its closer proximity to Ru. Strong H_2 adsorption on small Ru clusters explains the higher CO_2 methanation activity of Ru clusters on CeO_2 compared to a Ru step-edge surface, representative of Ru nanoparticles, where the H coverage is low due to stronger competition with adsorbed CO.

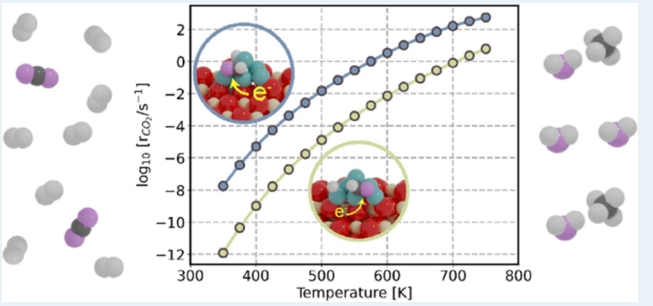

KEYWORDS: *CO_2 methanation, ruthenium, CeO_2, mechanism, density functional theory*

1. INTRODUCTION

Global warming is a primary driver for developing new sustainable fuel and chemical production technologies. The use of the greenhouse gas CO_2 as a carbon feedstock is also being considered in future scenarios.[1] CO_2 methanation ($CO_2 + 4\ H_2 \rightarrow CH_4 + 2\ H_2O$; the Sabatier reaction) can contribute to closing the carbon cycle when H_2 is produced from renewable sources. The Sabatier reaction is also of practical interest as it can be operated under mild conditions. Moreover, CH_4 is an energy carrier compatible with the current energy infrastructure. CO is often a byproduct of the Sabatier reaction, so it is important to develop catalysts that achieve a high selectivity to CH_4. CO_2 methanation can be catalyzed by transition metals such as nickel, cobalt, and ruthenium supported on metal oxides, carbides, and carbon supports.[2−13]

Ru supported on CeO_2 is a promising catalyst for the Sabatier reaction because it combines the excellent performance of Ru with oxygen vacancies in CeO_2, which can play a role in activating CO_2.[4,5,12] The activity and product distribution of metal-catalyzed reactions depend typically strongly on the size of the metal particles. They can be further modified by changing the extent of metal−support interactions.[12,14,15] While intrinsically, the activity of Ru for CO_2 methanation decreases when the Ru particles become smaller,[16] the use of CeO_2, which can create specific interfacial sites with the metal, leads to different reaction mechanisms. By enhancing the dispersion of Ru nanoparticles and promoting stronger support−metal interactions, the activity of CO_2 methanation can be improved. Furthermore, oxygen vacancies can be adsorption sites for CO_2, further enhancing the overall reaction rate.[17] Using operando spectroscopy, Wang et al. demonstrated that CO_2 methanation proceeds via the formate pathway on Ru/CeO_2, whereas it follows the carbonyl pathway on Ru/Al_2O_3.[18] The reducible nature of CeO_2 implies the presence of oxygen vacancies, which were found to play a crucial role in facilitating the conversion of formate to adsorbed methanol, which would then undergo further conversion to CH_4. A study of the influence of Ru loading in Ru/CeO_2 found that an intermediate Ru loading of 1 wt % led to the highest activity, which was linked to the highest concentration of oxygen vacancies.[19] In situ DRIFTS revealed

Received: August 10, 2023
Revised: October 19, 2023
Accepted: October 30, 2023
Published: November 9, 2023

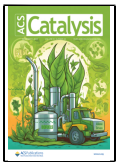

https://doi.org/10.1021/acscatal.3c03742
ACS Catal. 2023, 13, 15230−15247

that the reaction mechanism of CO_2 methanation is temperature sensitive. The reaction predominantly follows the carbonyl route at low temperatures, while the formate route was dominant at higher temperatures.[19] As activity appears to benefit from a higher concentration of oxygen vacancies, doping of CeO_2 with other metals has also been explored.[20−23] One such case pertains to the doping of Ru in the CeO_2 lattice.[4,12,24] Besides the role of oxygen vacancies, the size of the supported Ru particles will also affect the catalytic performance. It has been shown that single atoms of Ru on CeO_2 are highly selective to CO, i.e., they do not produce CH_4.[12,14] Guo et al. speculated that the size-dependent selectivity is due to strong metal−support interactions and H spillover being affected by the size of Ru.[12] A similar impact of the size of the metal phase has been observed for Rh/TiO_2, where it was found that a single atom of Rh on TiO_2 cannot adsorb both H_2 and CO, thereby preventing further hydrogenation of CO.[25]

Despite the interest in Ru/CeO_2 catalysts for CO_2 methanation, there needs to be a more detailed mechanistic understanding of the nature of the active sites, the reaction mechanisms, and the role of oxygen vacancies. Herein, we addressed these aspects by carrying out DFT calculations for the Sabatier reaction on three models for Ru/CeO_2. The first model represents single Ru atoms on CeO_2, for which we expect to have CO as the dominant product. The other two models involve a Ru_6 cluster to describe very small particles of Ru on stoichiometric CeO_2 and CeO_2 in which a Ru atom substitutes for a Ce atom. For CeO_2, the most thermodynamically stable (111) surface was chosen. The complete reaction energetics for the two latter models active in CO_2 methanation were used to perform comprehensive microkinetics simulations of CO_2 methanation.

2. METHODS

2.1. DFT Calculations. Spin-polarized density functional theory (DFT) calculations were performed using the VASP software (version 5.4.1)[26−28] with the Perdew−Burke−Ernzerhof (PBE)[29] exchange-correlation functional. The interactions between the core and electrons were treated using the projector-augmented wave method.[30−32] A cutoff energy of 400 eV was used after the optimization of surface models. Exploration of the effect of the cutoff energies on the total electronic energy, wherein we sampled cutoff energies between 400 and 600 eV, revealed that the total electronic energy was already sufficiently converged at a value of 400 eV, i.e., yielding energy differences smaller than 0.001 eV/atom (Table S1). To adequately describe the electron localization in the Ce 4f orbital, an on-site Coulomb repulsion as described by the Hubbard U parameter as Dudarev et al. introduced.[33] The U value was set to 5.0 eV for the Ce 4f orbitals, which lies in the range of 3.5−5.5 eV, providing sufficient localization of the electrons left upon oxygen removal from CeO_2.[34−38] The maximum force criterion for ionic convergence was set to 0.05 eV/Å. van-der-Waals interactions were considered using the DFT-D3 method with Becke−Jonson damping.[39,40] All the transition states were determined using the climbing image nudge elastic band (CI-NEB) method[41] and confirmed by vibrational analysis with a single imaginary frequency in the direction of the reaction coordinate. The Hessian matrix constructed for the vibrational analysis was based on a finite-difference approach by perturbation of the atomic positions by 0.01 Å. Adsorption energy, activation energy, and reaction energy were reported, including a zero-point energy correction.

The bonding and antibonding states were analyzed using a projected crystal orbital Hamiltonian population implemented in the LOBSTER software.[42,43] To investigate the redistribution of electron density of HCO* adsorbed on different models, atomic charges were calculated using the Bader charge decomposition scheme.[44]

The oxygen vacancy formation energy was calculated by

$$E_{O,v} = E_{def} + E_{H_2O} - E_{sto} - E_{H_2} \quad (1)$$

in which E_{def} and E_{sto} refer to the energy of defective surface and stoichiometric surface. E_{H_2O} and E_{H_2} are the energy of H_2O and H_2 in the gas phase.

The optimized CeO_2 lattice parameter is 5.49 Å, which agrees well with the experimental value (a = 5.41 Å).[45] The (111) surface of CeO_2 was adopted in our calculation because it is the most stable surface.[46−50] A surface model containing three O−Ce−O triple-layers with (4 × 4) supercells was built, and a vacuum layer of 15 Å was added to mitigate the interaction between neighboring supercells. The bottom O−Ce−O layer was fixed, while the top two O−Ce−O layers were allowed to relax. For the k-point sampling, only the gamma point was used. A Gaussian smearing width of 0.05 eV was adopted to determine the partial occupancies.

2.2. Microkinetics Simulations. Microkinetics simulations based on DFT-derived parameters were conducted to determine the most likely pathway for CO_2 methanation. For each elementary reaction step in the chemokinetic network, as given by

$$\nu_a A + \nu_b B \underset{k^-}{\overset{k^+}{\rightleftharpoons}} \nu_c C + \nu_d D \quad (2)$$

A corresponding rate expression, i.e., an ordinary differential equation in time, can be constructed as given by

$$r_A = -\frac{d[A]}{dt} = \nu_a(k^+[A]^{\nu_a}[B]^{\nu_b} - k^-[C]^{\nu_c}[D]^{\nu_d}) \quad (3)$$

Herein, ν_x is the stoichiometric coefficient of component X and $k^{\pm}$ is the rate constant for the forward and backward reaction. From transition state theory, the reaction rate constants are calculated by the Eyring equation:

$$k = \frac{k_B T}{h}\frac{f^{\#}_{TS}}{f_{IS}}\exp\left(-\frac{\Delta E_{act}}{k_B T}\right) \quad (4)$$

where h is the Planck constant, ΔE_{act} is the activation energy, k_B is the Boltzmann constant, T is the temperature, $f^{\#}_{TS}$ and f_{IS} are the partition function of the transition and initial states, respectively.

For the adsorption steps, it is assumed that the adsorbed molecule loses one of the translational degrees of freedom concerning the initial state. The rate of adsorption is determined by the rate of surface impingement of gas-phase molecules for nonactivated molecular adsorption:[51]

$$k_{ads} = \frac{PA}{\sqrt{2\pi m k_B T}} \quad (5)$$

P is the partial pressure of the adsorbate in the gas phase, A is the effective surface area of the adsorption site, and m is the mass of the adsorbate.

https://doi.org/10.1021/acscatal.3c03742
ACS Catal. 2023, 13, 15230−15247

Considering the reversibility of the adsorption step, the molecule regains all its rotational degrees of freedom (i.e., three degrees of freedom for nonlinear molecules and two degrees of freedom for linear molecules) and two translational degrees of freedom in the desorption step. Therefore, the desorption rate is given by

$$k_{\mathrm{des}} = \frac{k_{\mathrm{B}}T}{h}\frac{q_{\mathrm{vib,gas}}q_{\mathrm{rot,gas}}q_{\mathrm{trans2D,gas}}}{q_{\mathrm{vib,ads}}}\exp\left(\frac{\Delta E_{\mathrm{ads}}}{k_{\mathrm{B}}T}\right) \quad (6)$$

where ΔE_{ads} is the adsorption energy. $q_{\mathrm{vib,\ gas}}$, $q_{\mathrm{rot,\ gas}}$ and $q_{\mathrm{trans2D,\ gas}}$ represent the vibrational, rotational, and two-dimensional translation partition function of a molecule in the gas phase, respectively. $q_{\mathrm{vib,\ ads}}$ refers to the vibrational partition function of a molecule upon adsorption.

The microkinetics simulations were conducted in the temperature range 350−750 K, encompassing a wider range than typical conditions used in experiments. The gas phase contained a mixture of CO_2 and H_2 in a 1:4 ratio at a total pressure of 1 atm, which was chosen from experimental literature.[4] The pressures of CO, CH_4, and CH_3OH were set to zero. In all simulations, the gas-phase composition was kept constant and the simulations were carried out at zero conversion. At t = 0, the surface models did not contain any adsorbates. Time integration of the ordinary differential equations was performed using the backward differential formula method, as implemented in MKMCXX, until a steady state was obtained.[52] The relative and absolute tolerances were both set to 10^{-8}. The calculated pre-exponential factors are shown in Tables S2 and S3.

To identify the elementary reaction steps that control the overall rate of CO_2 consumption, Campbell's degree of rate control (DRC) analysis was employed.[53] All microkinetics simulations were conducted using the in-house-developed MKMCXX program. Herein, the overall rate for CO_2 conversion as a function of temperature is calculated by time-integrating the set of ordinary differential equations corresponding to the elementary reaction steps in the chemokinetic network.

For a reaction given by

$$\nu_R R \rightleftarrows \nu_{P_1}P_1 + \nu_{P_2}P_2 + \cdots + \nu_{P_i}P_i \quad (7)$$

the selectivity of P_i is calculated by the following equation:

$$\eta_{P_i} = \frac{\nu_{P_i}r_{P_i}}{\nu_R r_R} \quad (8)$$

where ν_R represents the stoichiometric coefficient of component R, r_{P_i} represents the production rate of product P_i, and r_R represents the reaction rate of the reactant.

3. RESULTS AND DISCUSSION

3.1. Ru/CeO_2 Models. Two distinct catalyst models featuring highly dispersed Ru/CeO_2 were created through the deposition of Ru single atoms and Ru_6 clusters onto the $CeO_2(111)$ surface (denoted as Ru_1/CeO_2 and Ru_6/CeO_2, respectively). Furthermore, one of the Ce was replaced by Ru in the Ru_6/CeO_2 model.

In search of a Ru_6/CeO_2 structure, we manually built 10 models with different initial Ru atomic arrangements and allowed for optimization. The resulting configurations and relative energies are collected in Figure S1. The most stable structure is shown in Figure 1. Based on DDEC6 charge analysis, the net charges on the CeO_2 support and the Ru_6 cluster are −0.35 |e⁻| and +0.35 |e⁻|, respectively.[54] Our results are consistent with XPS findings that Ru is positively charged in Ru/CeO_2 with electrons transferring from the Ru cluster to the CeO_2 support.[5] As CeO_2 is a reducible support and oxygen vacancies are involved in various reactions of practical importance,[5,18] the oxygen vacancy formation energy referenced H_2O product is calculated, before exploring the mechanism of CO_2 methanation. The oxygen vacancy formation energies given in Figure 2 show that it is more challenging to remove oxygen atoms directly bound to the Ru_6 clusters in Ru_6/CeO_2 than those located further away from the cluster and oxygen atoms on the pure $CeO_2(111)$ surface ($E_{\mathrm{O,v}}$ = −0.14 eV). The oxygen vacancies for the Ru_6/CeO_2 model are present in the outermost oxygen layer of CeO_2.

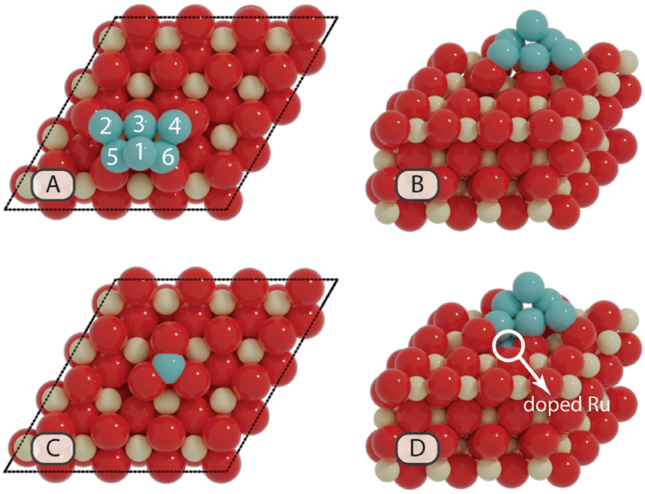

Figure 1. Most stable structure of Ru_6/CeO_2 (A: top view; B: side view), Ru_1/CeO_2 (C), and $Ru_6/RuCe_{x-1}O_{2x-1}$ (D).

To identify the most stable Ru-doped Ru_6/CeO_2 surface, we replaced different Ce ions in the top layer of the $CeO_2(111)$ surface by a Ru atom ($Ru_6/RuCe_{x-1}O_{2x}$). Figure S3A shows the relative energies for various locations of the Ru-for-Ce substitution, and Figure S3B shows the most stable structure. The doping of Ru has a negligible effect on the morphology of the Ru_6 cluster. The doping of metals into the CeO_2 lattice typically decreases the oxygen vacancy formation energy.[55] Figure 2B shows that a lower energy is required to remove the O atoms close to the Ru cluster in $Ru_6/RuCe_{x-1}O_{2x}$. Furthermore, we find that the oxygen vacancy is preferentially located below the surface, which is different from another theoretical study in which the CeO_2 support in Ru/CeO_2 was doped with Cr ($Ru/CrCeO_2$).[23] To verify that the subsurface location of the oxygen vacancy is due to the Ru dopant, we also computed the location and formation energy of oxygen vacancies for Ru-doped $CeO_2(111)$, i.e., a model without a Ru_6 cluster. As shown in Figure 2C, the formation of oxygen vacancies below the surface is more favorable than the formation of oxygen vacancies in the topmost layer. Therefore, $Ru_6/RuCe_{x-1}O_{2x}$ with a subsurface oxygen vacancy (denoted as $Ru_6/RuCe_{x-1}O_{2x-1}$) will be employed to explore the reaction mechanisms of the CO_2 hydrogenation. The interaction energies of the Ru_6 cluster on the CeO_2 and $RuCe_{x-1}O_{2x-1}$ surfaces are −11.28 and −12.08 eV, respectively, which indicates that Ru doped in the CeO_2 surface can stabilize Ru clusters on the surface.

https://doi.org/10.1021/acscatal.3c03742
ACS Catal. 2023, 13, 15230−15247

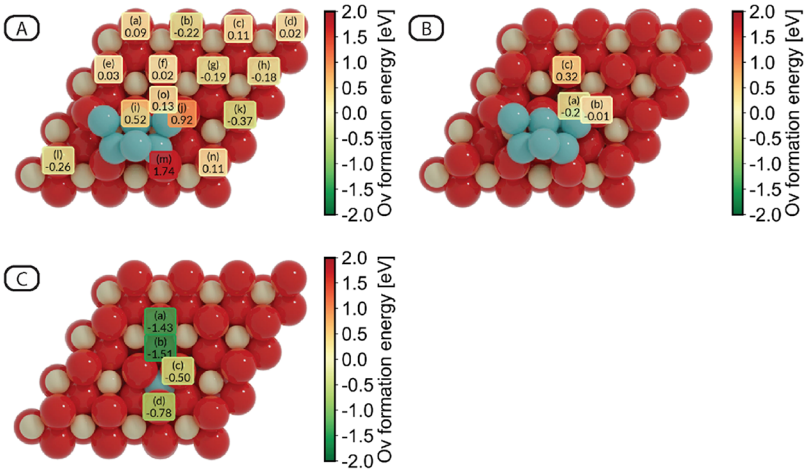

Figure 2. Heatmap of oxygen vacancy formation energy on (A) $Ru_6/CeO_2(111)$, (B) $Ru_6/RuCe_{x-1}O_{2x}(111)$, and (C) Ru doped $CeO_2(111)$ surface.

Previous studies have consistently demonstrated that the most stable configuration for the Ru_1/CeO_2 system involves the adsorption of a single Ru atom on the hollow site formed by three surface O atoms in CeO_2.[56−58] The optimized configuration of this structure is shown in Figure 1C.

3.2. Pathways of CO_2 Methanation. By employing the most stable structure of Ru_6/CeO_2, $Ru_6/RuCe_{x-1}O_{2x-1}$, and Ru_1/CeO_2, the CO_2 hydrogenation mechanism will be explored in detail. The 6 Ru atoms are labeled, as shown in Figure 1A. In the following description of the elementary reaction steps for the Ru_6 cluster models, we use the following formalism to describe the different adsorption modes on top (T), bridge (B), and hollow (H) sites. For instance, T_1 indicates the top site of Ru-1, B_{1-2} is the bridge site between Ru-1 and Ru-2, while H_{1-2-5} stands for the hollow site of Ru-1, Ru-2, and Ru-5.

3.2.1. CO_2 Methanation on Ru_6/CeO_2. We first compare different adsorption sites for CO_2 on the Ru cluster, the CeO_2 support, and the interface between the Ru cluster and the CeO_2 support. The results are summarized in Figure 3. When adsorbed on CeO_2 in the Ru_6/CeO_2 model (Figure 3E and F), CO_2 retains a linear configuration with slightly negative adsorption energy, comparable to the CO_2 adsorption energy on the bare $CeO_2(111)$ surface.[59] The adsorption mode changes when CO_2 is adsorbed at the interface between the Ru_6 cluster and CeO_2. Figure 3H shows that CO_2 interacts with a lattice O atom at the interface, forming a carbonate species with an adsorption energy of −0.38 eV. The adsorption of CO_2 on the Ru cluster exhibits a higher affinity in comparison to both the CeO_2 support and the Ru/CeO_2 interface. In the most stable configuration of CO_2 adsorption, it adopts a bent structure at a B_{1-2} site of the Ru cluster with an adsorption energy of −1.49 eV. Upon the adsorption, the C−O bonds in CO_2 are elongated to 1.26 and 1.27 Å, compared to the typical bond length of 1.18 Å observed in the gas phase.

H_2 adsorption becomes stronger in the order: CeO_2 support (Figure 3L) ∼ Ru_6−CeO_2 interface (Figure 3M) < molecular adsorption on Ru_6 (Figure 3I,K) < dissociative adsorption on Ru_6 cluster (Figure 3J,N,O,P). The most stable configuration of H_2 adsorption is associated with an adsorption energy of −1.11 eV. After adsorption, H_2 dissociates into two H* atoms at the B_{2-3} and B_{3-4} sites. During the CI-NEB calculation, it

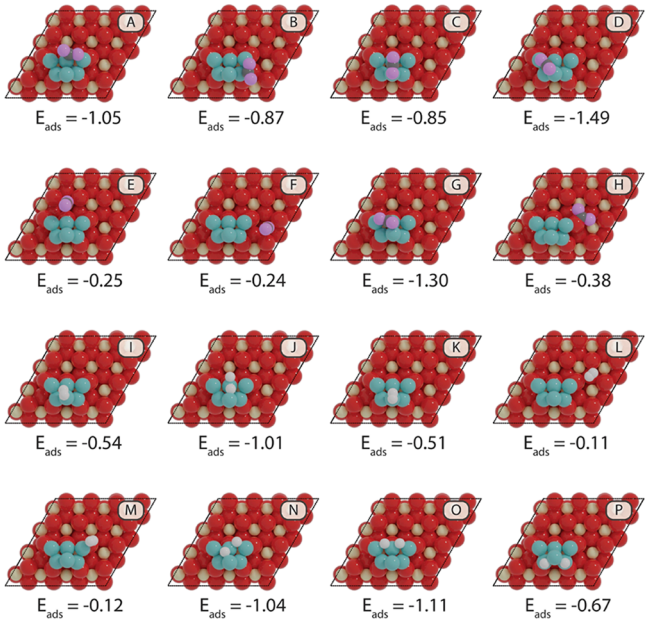

Figure 3. CO_2 (A−H) adsorption configurations and H_2 (I−P) on Ru_6/CeO_2. The adsorption energies are given in eV and include zero-point energy corrections.

was found that H_2 dissociates spontaneously (Figure 3I−O). We specify that all H_2 adsorption processes discussed herein are dissociative, and for brevity, we solely report the corresponding adsorption energies as the associated activation energies are found to be negligible. The preferential adsorption of CO_2 and H_2 on the Ru_6 cluster indicates that the hydrogenation of CO_2 will predominantly occur on the Ru_6 cluster.

For investigating the mechanisms of CO_2 methanation, we included several pathways, namely, (i) the direct CO_2 dissociation pathway, (ii) indirect CO_2* dissociation pathways involving HCOO* and COOH* intermediates, and (iii) a Mars−Van Krevelen reaction mechanism where an oxygen vacancy in the CeO_2 support is involved in CO_2* dissociation. The activation energies for all elementary steps are shown in Figure 4 in the form of a reaction network. Forward and backward activation energies are provided for every elementary reaction step. Every step is enumerated, and the corresponding

https://doi.org/10.1021/acscatal.3c03742
ACS Catal. 2023, 13, 15230−15247

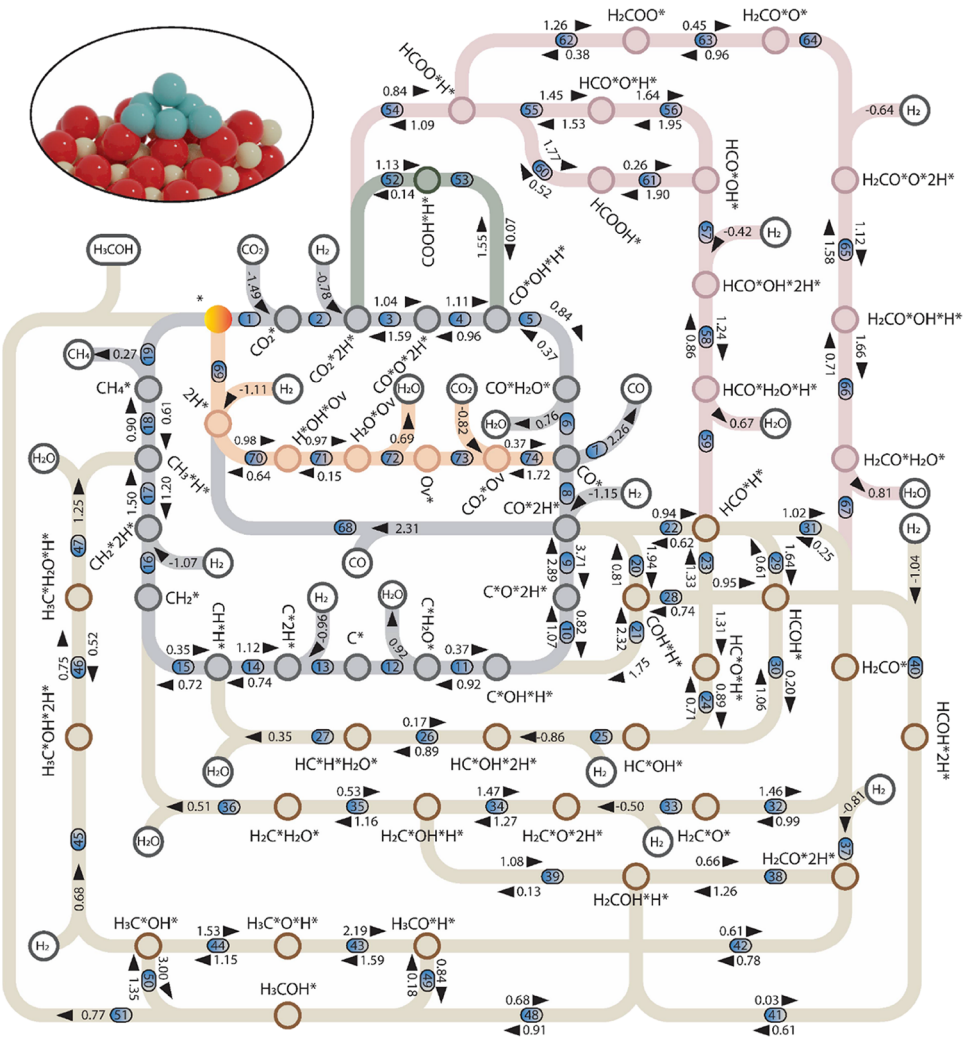

Figure 4. Reaction network of CO_2 methanation on Ru_6/CeO_2. Hollow nodes represent the reactants and products. Filled nodes represent the surface intermediates. Different reaction mechanisms are shown with different colors. The reaction numbers are shown as gradient blue ellipses. Unit in this figure: eV. In our main text, we utilize the notation R (followed by the reaction number) to indicate the specific step under discussion. This notation allows for clear and concise reference to individual reactions throughout the text.

reaction intermediates are depicted in the Supporting Information (Figures S5−S9). Direct scission of one of the C−O bonds in adsorbed CO_2* leads to adsorbed CO* and O* (CO_2 direct dissociation pathway). H-assisted CO_2 dissociation involves the hydrogenation of O or C in adsorbed CO_2* leading to COOH* (the COOH pathway) or HCOO* (formate pathway) intermediates. COOH* can be readily dissociated into CO* and OH*. The dissociation of HCOO* leads to HCO* and O*.[18,24] Another CO_2 dissociation pathway via a Mars-van Krevelen mechanism involves an oxygen vacancy in the support. The formation of oxygen vacancies in the CeO_2 surface can be facilitated by spillover H from metal particles.[60]

Direct Dissociation of CO_2. The CO_2 direct dissociation pathway is shown as the gray and brown paths in Figure 4. The adsorption energy of H_2 on the surface containing CO_2* is −0.78 eV. The direct dissociation of CO_2* leads to CO* and O* (ΔE_{act} = 1.04 eV, ΔE_R = 0.55 eV). Adsorbed O* then proceeds with two-step protonation to OH* (ΔE_{act} = 1.11 eV, ΔE_R = 0.15 eV) and H_2O* (ΔE_{act} = 0.84 eV, ΔE_R = 0.47 eV). The desorption of H_2O costs 0.76 eV, and the desorption of CO (R7) costs 2.26 eV.

The cleavage of CO* can occur through direct dissociation or dissociation upon the hydrogenation of CO*. The adsorption energy of H_2 is −1.15 eV. Direct dissociation of CO* proceeds by overcoming a high activation energy of 3.71 eV, representing the highest activation energy in the reaction mechanism network (Figure 4). The resulting C* atom is located at H_{1-4-5}, while the resulting O* atom is located at a B_{1-2} site. O* and C* hydrogenations lead to the formation of H_2O and CH_4, respectively. For the hydroxyl formation, the H* on B_{1-6} first migrates to B_{1-5} (ΔE_R = 0.24 eV), followed by hydroxyl formation (ΔE_{act} = 0.58 eV, ΔE_R = 0.02 eV). Migration of H* from T_4 to B_{1-5} occurs so that the H* is close to the hydroxyl (ΔE_R = −0.51 eV). Recombination of OH* and H* leads to adsorbed H_2O* (ΔE_{act} = 0.92 eV, ΔE_R = 0.55 eV). The desorption of H_2O costs 0.86 eV, leaving only adsorbed C* at H_{1-3-4}. H_2 will then adsorb at B_{2-3} and B_{1-5} (ΔE_{ads} = −0.96 eV), providing H* for forming CH* with an activation energy of 0.74 eV. The final state is more stable than the initial state by 0.32 eV. Migration of the other H* over the cluster is required to form CH_2*, which is slightly exothermic by 0.06 eV. Then, CH* reacts with H* to form CH_2* with activation and reaction energies of ΔE_{act} = 0.72 and ΔE_R =

https://doi.org/10.1021/acscatal.3c03742
ACS Catal. 2023, 13, 15230−15247

0.37 eV, respectively. Another H_2 adsorption is associated with an adsorption energy of −1.07 eV to hydrogenate CH_2* to give CH_3* and CH_4*. The activation and reaction energies for CH_3* formation are ΔE_{act} = 1.50 eV and ΔE_R = 0.30 eV, respectively. The subsequent addition of H* leading to CH_4* has an activation energy of 0.90 eV and is endothermic by 0.29 eV. Finally, CH_4 desorbs into the gas phase with a minor energy penalty of 0.27 eV. The overall reaction energy for CO_2 methanation is −1.75 eV, which reasonably agrees with the experimental enthalpy change of −1.71 eV.[61]

Direct C−O bond dissociation in adsorbed CO* is the most difficult elementary reaction step along the pathway to CH_4. Direct CO* dissociation mechanism is preferred over hydrogen-assisted CO* dissociation on, for instance, the stepped Ru(11−21) surface.[62] In contrast, CO* dissociation via CO* → COH* → HCOH* → CH* + OH* is more plausible on the planar Ru (0001) surface.[63] As the mode of the CO* dissociation on the Ru cluster is unclear, H-assisted C−O bond dissociation mechanisms were also explored. There are two pathways for H-assisted C−O dissociation: hydrogenation of C in CO* to form HCO* and hydrogenation of O in CO* to form COH*. The activation and reaction energies for COH* and HCO* formation are ΔE_{act} = 1.94 eV, ΔE_R = 1.13 eV, ΔE_{act} = 0.94 eV, and ΔE_R = 0.32 eV, respectively. This means that the formation of HCO* is energetically favored. COH* leads to the formation of C* and OH* (R21). The activation and reaction energies of this step are ΔE_{act} = 1.75 eV and ΔE_R = −0.57 eV, respectively. The final state is the same as the C*OH*H* state in the direct CO* dissociation pathway. The overall activation energy of dissociation of CO* via COH* is 2.88 eV, which is lower than the activation energy of its direct dissociation. HCO* formation is followed by HCO* dissociation (ΔE_{act} = 1.31 eV, ΔE_R = 0.08 eV), HCOH* formation (ΔE_{act} = 1.64 eV, ΔE_R = 1.03 eV) or H_2CO* formation (ΔE_{act} = 1.02 eV, ΔE_R = 0.77 eV). Considering the formation of HCO*, the overall activation energy of the dissociation of the CO* via HCO* intermediate species is 1.63 eV, much lower than the overall activation energy of direct CO* dissociation (ΔE_{act} = 3.71 eV) and COH* dissociation (ΔE_{act} = 2.88 eV). Migration of H* from B_{1-6} to B_{1-5} is necessary for forming OH* (ΔE_R = −0.11 eV), leading to a more stable HCO*H* state. OH* formation requires overcoming an activation energy of 0.89 eV with an exothermic reaction energy of 0.18 eV (R24). Note that the HC*OH* species can be alternatively formed via dissociation of HCOH*, which can be obtained via hydrogenation of COH* (R28, ΔE_{act} = 0.95 eV, ΔE_R = 0.21 eV) or protonation of HCO* (R29, ΔE_{act} = 1.64 eV, ΔE_R = 1.03 eV). HCOH* dissociation (R30) proceeds by overcoming an activation energy of ΔE_{act} = 0.20 eV, and this step is highly exothermic by 1.73 eV. The adsorption of H_2 on the surface containing CH* and OH* is exothermic by −0.86 eV (R25). H_2O* formation via a combination of OH* and H* is endothermic by 0.72 eV and has an activation energy of 0.89 eV. Following the desorption of H_2O (ΔE_{ads} = −0.72 eV), CH* and H* species are retained on the Ru cluster. These species undergo migration to reach a more stable state, i.e., the CH*H* state (ΔE_R = −0.37 eV), which is also involved in the direct dissociation pathway. To link this latter state to the state before H_2O desorption, we combined the two steps and modified and adjusted the adsorption energy of H_2O to −0.35 eV, as depicted in Figure 4.

Besides the HCO* dissociation pathway, we also investigated pathways involving H_2CO* formation (R31, ΔE_{act} = 1.02 eV, ΔE_R = 0.77 eV) and dissociation (R32, ΔE_{act} = 0.99 eV, ΔE_R = −0.46 eV). After dissociation of H_2CO*, H_2 adsorbs on this surface with ΔE_{ads} = −0.50 eV. Then, O* is removed through the formation and desorption of H_2O. First, the O* protonation forming OH* (R34) has an activation energy of 1.27 eV and is exothermic by 0.20 eV. In the next step, H_2O* is formed (R35) with an activation energy of 1.16 eV and a reaction energy of 0.63 eV. Desorption of H_2O (ΔE_{ads} = −0.51 eV) leads to a CH_2* surface intermediate, which can be further hydrogenated to CH_4 according to the mechanism discussed above.

H_2CO* can also be hydrogenated to give H_3CO* or H_2COH*. The adsorption energy of H_2 on the surface that contains the H_2CO* intermediate is −0.81 eV. To protonate H_2CO* to H_2COH*, these two H* molecules migrate (ΔE_R = 0.17 eV). The forward activation energy for H_2COH* formation, including H* migration, is 1.26 eV (R38 in Figure 4). H_2COH* can also be obtained by the hydrogenation of HCOH*. H_2COH* formation from HCOH* (R41) requires an activation energy of ΔE_{act} = 0.61 eV and is endothermic by 0.58 eV. The H* atom is supplied by the adsorption of H_2 (R40) (ΔE_{ads} = −1.04 eV). Figure S6 shows the configurations involved in the conversion of HCOH* to H_2COH*. Dissociation of H_2COH* overcomes an activation energy of 0.13 eV, which is exothermic by 0.96 eV.

C-terminated hydrogenation of H_2CO* generates H_3CO* (ΔE_{act} = 0.78 eV, ΔE_R = 0.17 eV). Dissociation of H_3CO* generates adsorbed H_3C* and O* by overcoming an activation energy of 1.59 eV (ΔE_R = −0.60 eV). Afterward, the combination of O* and the remaining H* forms OH* (ΔE_{act} = 1.15 eV, ΔE_R = −0.38 eV). Two further H* atoms are provided by H_2 adsorption (ΔE_{ads} = −0.68 eV). The formation of H_2O* (R46) has an activation energy of 0.75 eV and is endothermic by 0.23 eV. H_2O desorption (ΔE_{ads} = −1.25 eV) leads to the same configuration as the CH_3*H* in the gray pathway. As CH_3OH was observed as a reaction product during CO_2 methanation on Ru/CeO_2,[18] we also studied the formation of H_3COH* (R49, ΔE_{act} = 0.84 eV, ΔE_R = 0.66 eV). The activation energy compares favorably with the activation energy for H_3CO* dissociation, indicating that this is a possible pathway to CH_3OH formation. Another pathway to obtain H_3COH* is via the hydrogenation of H_2COH* (R48, ΔE_{act} = 0.91 eV, ΔE_R = 0.23 eV). CH_3OH desorption (R51) costs 0.77 eV. Another possibility is that the C−O bond in CH_3OH is cleaved (R50, ΔE_{act} = 1.35 eV, ΔE_R = −1.65 eV).

The energy diagrams for direct and H-assisted CO* dissociation are shown in Figure 5. Direct dissociation of CO* must overcome an activation energy of 3.71 eV. The overall activation energies for H-assisted CO* dissociation via COH*, HCO*, HCOH* (CO* → HCO* → HCOH*), HCOH* (CO* → COH* → HCOH*), H_2CO*, H_3CO*, H_2COH*, and H_3COH* are 2.88 1.63, 1.96, 2.07, 2.08, 1.76, 1.54, and 2.18 eV, respectively. H-assisted CO* dissociation pathways have lower activation energies than direct CO* dissociation. H-assisted CO* dissociation pathways via HCO* and H_2COH* are preferred over the other pathways.

Carboxyl Pathway. In this pathway, CO_2* reacts with H* to form COOH* (R52 in Figure S8) by overcoming an activation energy of 1.13 eV. This step is highly endothermic by 1.01 eV. Following the rotation of COOH* (ΔE_R = −0.02 eV), the subsequent dissociation of COOH* leads to the

https://doi.org/10.1021/acscatal.3c03742
ACS Catal. 2023, 13, 15230−15247

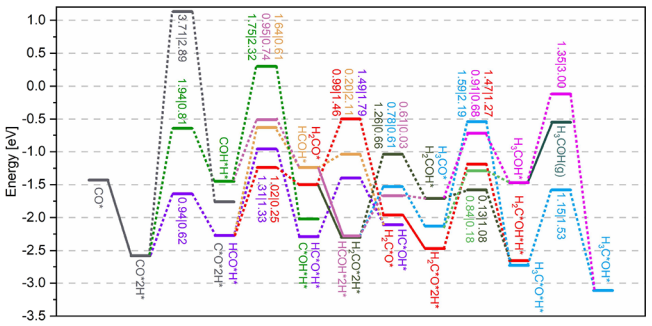

Figure 5. Energy diagram of direct and H-assisted CO* dissociation on Ru_6/CeO_2. Solid lines between two species indicate the adsorption and desorption steps, and the dotted lines refer to surface reactions involving transition states. The values above and below the separated lines are the activation energy for the forward and backward reactions.

prompt formation of CO* and OH* with a remarkably low activation energy of 0.07 eV (ΔE_R = −1.48 eV). This configuration is the same as that of CO*OH*H in Figure S5.

Formate Pathway. In many experimental studies, formate (HCOO*) has been observed as a reaction intermediate,[4,18,23] therefore also considered here. Upon HCOO* formation (ΔE_{act} = 0.84 eV, ΔE_R = −0.25 eV), the two C−O bonds in adsorbed formate are elongated to 1.27 and 1.28 Å (compared to 1.18 Å in the gas phase). We considered three branches for its further conversion: HCOO* dissociation, HCOOH* formation, and H_2COO* formation. Dissociation of HCOO* results in HCO* and O* (ΔE_{act} = 1.45 eV, ΔE_R = −0.08 eV), and the O* can be removed through the formation and subsequent desorption of H_2O. The first step toward H_2O formation is the protonation of O*, with activation and reaction energies of ΔE_{act} = 1.64 eV and ΔE_R = −0.31 eV, respectively. This is followed by the exothermic adsorption of H_2 (ΔE_{ads} = −0.42 eV). The formation of H_2O* then required an activation energy of 1.24 eV. H_2O desorption (ΔE_{ads} = −0.67 eV) leads to HCO* and H* in Figure S6. In addition to HCOO* dissociation, another pathway involves HCOO* protonation to form HCOOH* (R60, ΔE_{act} = 1.77 eV, ΔE_R = 1.25 eV). Protonation of HCOO* further activates the C−O bond. Dissociation of HCOOH* requires a low activation energy of 0.26 eV to generate HCO* and OH* (R61, ΔE_R = −0.19 eV). Conformational changes of HCO* and OH* on the Ru cluster led to the same configuration as generated by R56. These rearrangements are exothermic by 1.45 eV.

The third branch involving HCOO* reacts with another adsorbed H* to form H_2COO* (R62, ΔE_{act} = 1.26 eV, ΔE_R = 0.88 eV). The resulting intermediate has an elongated C−O bond length of 1.42 Å. H_2COO* dissociation (R63) to generate H_2CO* and O* proceeds with a relatively lower activation energy of 0.45 eV (ΔE_R = −0.51 eV). The resulting O* can be hydrogenated to H_2O*. H_2 adsorbs on the Ru cluster with an adsorption energy of −0.64 eV. The two hydrogenation steps of O* to form OH* and H_2O* involve activation and reaction energies of ΔE_{act} = 1.12 eV, ΔE_R = −0.46 eV, and ΔE_{act} = 1.66 eV, ΔE_R = 0.95 eV, respectively. The involved intermediates occurring in reactions R65, R66, and R67 are depicted in Figure S8. Desorption of H_2O (ΔE_{ads} = −0.81 eV) generates the same configuration of H_2CO* in Figure S7.

Mars-van-Krevelen Mechanism. We also considered pathways involving an oxygen vacancy in the CeO_2 support. It can be seen in Figure 2 that the oxygen vacancy formation energy concerning H_2O formation in Ru_6/CeO_2 is in the range of −0.37 to 1.74 eV. In comparison, it is only −0.14 eV for the stoichiometric $CeO_2(111)$ surface. This means that some O atoms can be more easily removed, but also bits that are more difficult to remove due to the presence of the Ru cluster. The CeO_2 lattice O atoms connected with the Ru_6 cluster typically have positive energies for vacancy formation. The O atom labeled *k* has the lowest oxygen vacancy formation energy (Figure 2A). Figure S4A shows that there exists 5 Ce^{3+} for the stoichiometric Ru_6/CeO_2 surface, reflecting that 5 electrons transferred from the Ru cluster to the CeO_2 support. Such electron transfer is commonly observed when metal clusters are deposited on CeO_2. For instance, placing a Au_6 cluster on $CeO_2(111)$ leads to 2 Ce^{3+} ions, while a Pd_8 cluster only reduces 1 Ce^{4+} ion to Ce^{3+}.[63,64] On the other hand, placing the Ni_5 cluster on the CeO_2 surface results in 5 Ce^{3+} ions.[65] The differences in electron transfer can be associated with differences in reactivity, with the more reactive metals Ru and Ni donating more electrons to the CeO_2 support than Pd and Au. The formation of an oxygen vacancy *k* leads to the further reduction of two more Ce^{4+} ions to Ce^{3+} ions, as shown in Figure S4b. This observation suggests that there is negligible electron transfer to the Ru_6 cluster.

We then investigated CO_2 adsorption on the surface with oxygen vacancy *k*, as shown in Figure S3. The adsorption energy of CO_2 in the O_v site is −0.49 eV, with CO_2 remaining linear, indicative of relatively weak adsorption. However, the CO_2 adsorption on the Ru cluster is exothermic by −1.51 eV, similar to the CO_2 adsorption on the stoichiometric Ru_6/CeO_2 surface (ΔE_{ads} = −1.49 eV). Considering that removal of oxygen *k* results in negligible changes in the morphology of the Ru_6 cluster, the charge distribution, and the CO_2 adsorption energy, it is reasonable to assume that the mechanism of CO_2

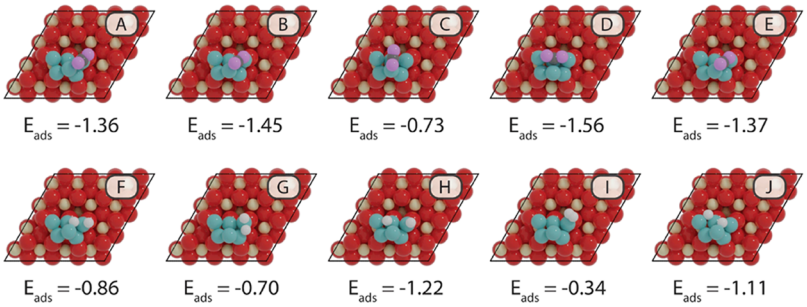

Figure 6. Configuration of adsorbed CO_2 (A−E) and adsorbed H_2 (F−J) on $Ru_6/RuCe_{x-1}O_{2x-1}$. The adsorption energies are given in eV and include zero-point energy corrections.

https://doi.org/10.1021/acscatal.3c03742
ACS Catal. 2023, 13, 15230−15247

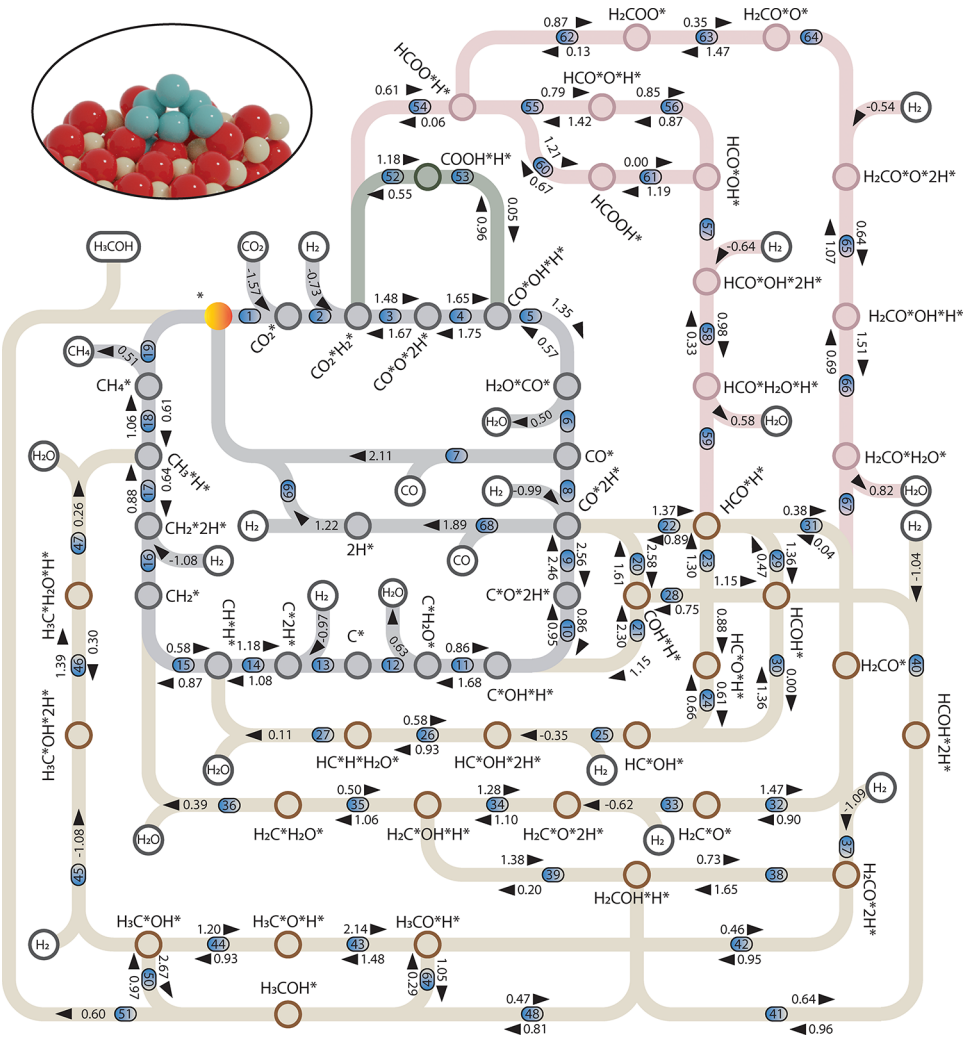

Figure 7. Reaction network for CO_2 methanation on the $Ru_6/RuCe_{x-1}O_{2x-1}$. Hollow nodes represent reactants and products. Filled nodes stand for the surface intermediates. Different reaction mechanisms are shown with different colors. The reaction numbers are shown in gradient blue ellipses. Unit in this figure: eV.

methanation on Ru_6/CeO_2 with an oxygen vacancy at position *k* is the same as that on the stoichiometric Ru_6/CeO_2 model.

We also explored the adsorption of CO_2 at an oxygen vacancy close to the Ru_6 cluster. Oxygen *i* exhibits the lowest oxygen vacancy formation energy among the oxygen atoms directly connected to the Ru atoms. The CO_2 adsorption at oxygen vacancy *i* is exothermic by 0.82 eV (Figure S3C). One O atom of CO_2* fills the oxygen vacancy, and the C atom coordinates with one of the interfacial Ru atoms. The adsorbed CO_2* can directly dissociate with an activation energy of 0.37 eV (R74, ΔE_R = −1.35 eV). The dissociation of CO_2* generates a lattice O atom that heals the oxygen vacancy while leaving CO* adsorbed on the Ru_6 cluster behind. This configuration is the same as that of CO*, shown in Figure S5.

To complete the catalytic cycle, the adsorption of H_2 (R69, ΔE_{ads} = −1.11 eV) and subsequent reaction with lattice O to form OH* and H_2O* are also computed (R70 and R71). OH* and H_2O* formation are endothermic by 0.34 and 0.82 eV with activation energies of 0.98 and 0.97 eV, respectively. The corresponding intermediate states are depicted in Figure S9. Desorption of H_2O generates an oxygen vacancy, costing 0.69 eV.

3.2.2. CO_2 Methanation on $Ru_6/RuCe_{x-1}O_{2x-1}$. Figure 6 shows the adsorption of CO_2 and H_2 on the $Ru_6/RuCe_{x-1}O_{2x-1}$ surface, which involves similar energetics as their adsorption on Ru_6/CeO_2. CO_2 and H_2 preferentially adsorb on the Ru cluster. CO_2* adopts a bent configuration in the most stable adsorption state (ΔE_{ads} = −1.56 eV) with an O−C−O angle of 126.2°, as shown in Figure 6D. Dissociative H_2 adsorption is spontaneous. In the most stable configuration, one H atom is located in the B_{2-3} site and the other H in the T_4 site with an adsorption energy of −1.22 eV.

Next, the mechanism of CO_2 methanation was explored for $Ru_6/RuCe_{x-1}O_{2x-1}$. The calculated activation energies and the corresponding surface intermediates are shown in Figures 7 and S10−S13, respectively.

Direct CO_2 Dissociation. In Figure 7, H_2 adsorbs on the $Ru_6/RuCe_{x-1}O_{2x-1}$ surface containing CO_2* with an adsorption energy of −0.73 eV. Direct dissociation of CO_2* yields adsorbed CO* and O* (ΔE_{act} = 1.48 eV and ΔE_R = −0.19 eV). The O* atom is removed through two-step protonation to H_2O*. In the first step, O* reacts with one H* to form OH* (ΔE_{act} = 1.65 eV, ΔE_R = 0.20 eV). In the second step, the other H* migrates to a position close to OH* (ΔE_R = −0.30 eV) and reacts with OH* to form H_2O* (ΔE_{act} = 1.35 eV, ΔE_R

https://doi.org/10.1021/acscatal.3c03742
ACS Catal. 2023, 13, 15230−15247

= 0.78 eV). Desorption of H_2O (ΔE_{ads} = −0.50 eV) results in a surface containing only adsorbed CO* at the B_{1-3} site. CO desorption costs 2.11 eV.

For the activation of CO*, both direct CO* dissociation and H-assisted CO* dissociation are considered. H_2 adsorption on the cluster containing CO* is exothermic by 0.99 eV. CO* dissociation results in C* and O* with an activation energy of 2.56 eV and a reaction energy of 0.10 eV. Compared to Ru_6/CeO_2 (ΔE_{act} = 3.46 eV for direct dissociation of CO*), the doping of Ru decreases the activation energy of CO* dissociation. Next, the O* atom is removed via the formation and desorption of H_2O. OH* formation (R10) requires overcoming an activation energy of 0.86 eV (ΔE_R = −0.09 eV). H* migration from B_{1-6} to B_{1-5} and OH* rotation occurs (ΔE_R = −0.26 eV), so H* ends up close to OH*. H_2O* formation is endothermic by 0.82 eV with an activation energy of 1.68 eV. Desorption of H_2O into the gas phase costs 0.63 eV. The remaining C* is located at the H_{1-3-4} site and undergoes stepwise hydrogenation with adsorbed H*. Adsorption of H_2 is exothermic by 0.97 eV (R13). Two H* atoms react with C* to generate CH* (ΔE_{act} = 1.08 eV, ΔE_R = −0.10 eV) and CH_2* (ΔE_{act} = 0.87 eV, ΔE_R = 0.29 eV). To further hydrogenate CH_2*, H_2 adsorption takes place (ΔE_{ads} = −1.08 eV). The formation of CH_3* is endothermic by 0.24 eV and overcomes an activation energy of 0.88 eV. In the next step, the CH_3* species reacts with the remaining H* to form CH_4* (ΔE_{act} = 1.06 eV, ΔE_R = 0.45 eV). As a final step, CH_4 desorption regenerates the initial surface (ΔE_{ads} = −0.51 eV).

H-assisted CO* dissociation mechanism is also considered for the $Ru_6/RuCe_{x-1}O_{2x-1}$ model. Figure S11 shows that HCO* formation (R22, ΔE_{act} = 1.37 eV, ΔE_R = 0.48 eV) is more favorable than COH* formation (R20, ΔE_{act} = 2.58 eV, ΔE_R = 0.97 eV). COH* dissociation yields C* and OH* (ΔE_R = −1.03 eV), overcoming an activation energy of 1.15 eV (R21). OH* and H* migration results in a more stable configuration (ΔE_R = −0.12 eV), the same as that of the C*OH*H* state in Figure S10. Once HCO* is formed, there are three possible reaction pathways: (i) HCO* dissociation (R23), (ii) HCO* protonation to HCOH* (R29), and (iii) hydrogenation of HCO* to H_2CO* (R31). HCO* dissociation forms HC* and O* (ΔE_{act} = 0.88 eV, ΔE_R = −0.43 eV). Then, O* reacts with the remaining H*, forming OH* (ΔE_R = −0.08 eV), overcoming an activation energy of 0.63 eV. The OH* species is subsequently removed by the formation of H_2O* (ΔE_{act} = 0.93 eV, ΔE_R = 0.35 eV), which involves the adsorption of H_2 (ΔE_{ads} = −0.35 eV). After H_2O desorption (ΔE_{ads} = −0.11 eV), CH* and H* remain on the Ru cluster, representing the same state as the CH*H* state in Figure S10. HCOH* species can be generated through HCO* protonation (R29, ΔE_{act} = 1.36 eV, ΔE_R = 0.89 eV) or COH* hydrogenation (R28, ΔE_{act} = 1.15 eV, ΔE_R = 0.40 eV). Considering the high activation energy for the formation of COH* (R20), it is likely that the formation of HCOH* via HCO* protonation is more favorable. HCOH* is a metastable species that dissociates spontaneously and represents the same HC*OH* state in the HCO* dissociation pathway with a highly exothermic reaction energy of 1.36 eV. The hydrogenation of HCO* to H_2CO* involves a relatively low activation energy of 0.38 eV. This step is endothermic by 0.34 eV. H_2CO* dissociates into H_2C* and O* (R32, ΔE_R = −0.57 eV) by overcoming an activation energy of 0.90 eV. Next, H_2 adsorption is exothermic by 0.62 eV. O* is removed by two-step protonation, which requires overcoming the activation energies of ΔE_{act} = 1.10 eV (R34) and ΔE_{act} = 1.06 eV (R35). The reaction energies for OH* formation and H_2O* formation are ΔE_R = −0.18 eV and ΔE_R = 0.56 eV. After H_2O desorption which costs 0.39 eV, CH_2* species remain. The hydrogenation of CH_2* to CH_4 follows the pathway discussed above.

H-assisted H_2CO* dissociation pathways were also investigated. H_2 adsorbs on the cluster containing H_2CO* are exothermic by 1.09 eV. The resulting two H* atoms are located at B_{1-6} and B_{1-2} sites. The former H* attacks the O atom in H_2CO*, resulting in H_2COH* (R38, ΔE_{act} = 1.65 eV, ΔE_R = −0.92 eV). Simultaneously, H* located at B_{1-2} undergoes migration to B_{2-3}. H_2COH* can be formed through an alternative pathway involving the hydrogenation of HCOH*. The adsorption energy of H_2 is −1.04 eV. The formation of H_2COH* hydrogenation via HCOH* hydrogenation (R41) needs to overcome an activation energy of 0.96 eV (ΔE_R = 0.32 eV). H_2COH* cleavage (R39) leads to H_2C* and OH* (ΔE_{act} = 0.20 eV, ΔE_R = −1.18 eV). The corresponding configurations illustrating these processes are depicted in Figures S11 and S12. Another option for H_2CO* hydrogenation is the formation of H_3CO* (R42, ΔE_{act} = 0.95 eV, ΔE_R = 0.49 eV). Next, H_3CO* undergoes a dissociation of its C−O bond, resulting in the formation of H_3C* and O* (R43, ΔE_{act} = 1.48 eV, ΔE_R = −0.66 eV). These species are then hydrogenated to yield CH_4 and H_2O, respectively. The H_3C* coordinates with one Ru atom in the top layer, and the O* locates at T_4. The activation and reaction energies for combining O* and H* to form OH* are ΔE_{act} = 0.93 eV and ΔE_R = −0.27 eV. One H_2 molecule is adsorbed further to remove OH* (ΔE_{ads} = −1.08 eV). The formation of H_2O* needs to overcome an activation energy of 1.39 eV with an endothermic reaction energy of 1.09 eV. After the desorption of H_2O (ΔE_{ads} = −0.26 eV), the reaction proceeds toward forming the CH_3*H* intermediate species via the direct CO* dissociation mechanism. A pathway alternative to H_3CO* dissociation involves the formation of CH_3OH (R49, ΔE_{act} = 1.05 eV, ΔE_R = 0.76 eV). CH_3OH is formed as a byproduct through desorption (ΔE_{ads} = −0.60 eV). CH_3OH dissociation (R50) yields the same configuration as H_3C*OH*. The activation energy and reaction energy for this step are ΔE_{act} = 0.97 eV and ΔE_R = −1.69 eV, respectively.

In summary, the direct dissociation of CO* dissociation requires an activation energy of 2.56 eV. The overall activation energies for H-assisted CO* dissociation via COH*, HCO*, HCOH* (via HCO*), H_2CO*, H_3CO*, H_2COH*, and H_3COH* are 2.58 1.37, 1.85, 1.72, 1.98, 1.65, and 2.23 eV, respectively. Therefore, it is speculated that H-assisted CO* dissociation via HCO* is the most likely pathway from the kinetic point of view.

Carbonxyl Pathway. The relevant configurations of the COOH pathway on $Ru_6/RuCe_{x-1}O_{2x-1}$ are depicted in Figure S13. H* reacts with CO_2* forming COOH* (ΔE_{act} = 1.18 eV, ΔE_R = 0.63 eV). C−O bond dissociation is facile after the formation of COOH* with an activation energy of 0.05 eV. This step is exothermic by 0.91 eV. Dissociation of COOH* produces the same surface intermediate of CO*OH*H* in the direct CO_2 dissociation pathway. The overall activation energy of CO_2* dissociation to generate CO*OH*H* via COOH* is 1.18 eV, whereas it is 1.65 eV in the competing pathway involving direct CO_2* dissociation. This indicates that the COOH* pathway is more favorable.

Formate Pathway. The hydrogenation of the carbon atom, resulting in the formation of formate (HCOO*), was also

https://doi.org/10.1021/acscatal.3c03742
ACS Catal. 2023, 13, 15230−15247

investigated and is depicted in Figure S13. The formation of HCOO* (R54) was found to be endothermic by 0.55 eV, accompanied by an activation energy of 0.61 eV. The activation energy for HCOO* formation is lower than those for the direct dissociation of CO_2* and the formation of COOH*, whereas HCOO* dissociation requires an activation energy of 0.79 eV (ΔE_R = −0.63 eV). Considering the endothermic nature of HCOO* formation, the overall activation energy for its formation and dissociation is 1.34 eV, which is higher than the overall activation energy of COOH* formation and dissociation. The O* species is then removed through the formation and desorption of H_2O. The activation and reaction energy for OH* formation are 0.85 and −0.02 eV, respectively. The OH* then reacts with H* supplied by H_2 adsorption (ΔE_{ads} = −0.64 eV), forming H_2O* (ΔE_{act} = 0.98 eV, ΔE_R = 0.65 eV). Desorption of H_2O (ΔE_{ads} = −0.58 eV) yields the same configuration of HCO*H* in Figure S12. Instead of HCOO* dissociation, HCOO* protonation results in the formation of a metastable species HCOOH* (R60, ΔE_{act} = 1.21 eV, ΔE_R = 0.55 eV), which spontaneously dissociates into HCO* and OH* (ΔE_R = −1.19 eV).

The formation of H_2COO* through HCOO* hydrogenation (ΔE_{act} = 0.87 eV, ΔE_R = 0.74 eV) further activates the C−O bond. An activation energy of 0.35 eV is involved in the subsequent dissociation of H_2COO* into H_2CO* and O* (ΔE_R = −1.12 eV). The O* atom will be removed via the formation and desorption of H_2O. The H* atoms stem from the dissociative adsorption of H_2 (ΔE_{ads} = −0.54 eV). The activation energies for forming OH* and H_2O* are 0.64 and 1.51 eV, respectively. Finally, the desorption of H_2O (ΔE_{ads} = −0.82 eV) results in the same configuration of H_2CO* as shown in Figure S12 (R67).

3.2.3. CO_2 Methanation on Ru_1/CeO_2. Figure 8 shows that CO_2 and H_2 adsorption on Ru_1/CeO_2 are associated with

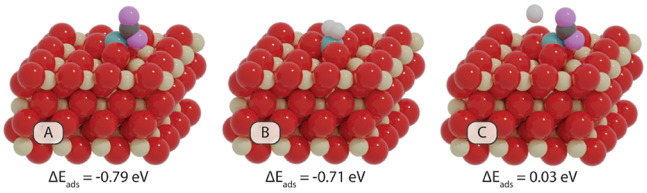

Figure 8. CO_2 (A) and H_2 (B) adsorption on Ru_1/CeO_2. (C) H_2 adsorption on Ru_1/CeO_2 containing CO_2.

adsorption energies of −0.79 and −0.71 eV, respectively. CO_2 adsorbs with the carbon atom coordinated to the Ru atom. One O atom is coordinated with Ru and Ce, and the other O atom points into the vacuum layer. H_2 adsorbs on the Ru atom with a H−H distance of 0.86 Å. The H_2 adsorption energy after CO_2 is adsorbed slightly positive (ΔE_{ads} = 0.03 eV), implying that the coadsorption of CO_2 and H_2 on the Ru single atom is hindered. We explored the possibility of H_2 spillover by considering the formation of two OH groups and subsequent adsorption of CO_2 on the Ru atom. The potential energy diagram associated with these steps is given in Figure 9. The migration of one H atom to a CeO_2 lattice O atom leads to an OH group adjacent to the Ru atom, leaving an H* species behind on the single Ru atom (ΔE_{act} = 0.93 eV, ΔE_R = −0.32 eV). The subsequent migration of the second H* atom results in another adjacent OH group (ΔE_{act} = 1.39 eV, ΔE_R = 0.58 eV). CO_2 adsorption on this structure is favorable (ΔE_{ads} = −1.41 eV) compared with the case where Ru is coordinated

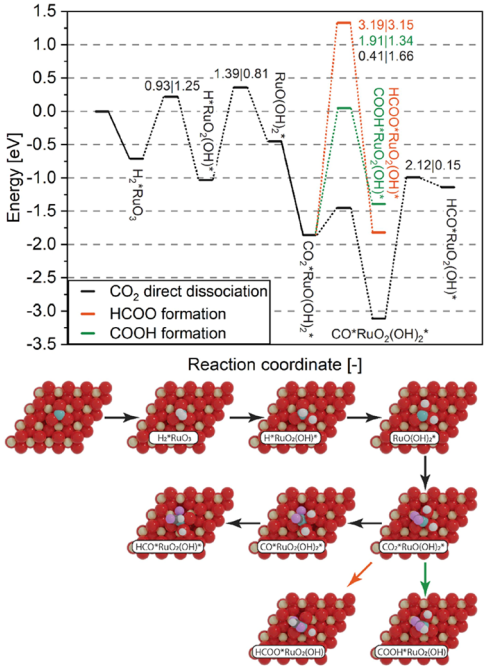

Figure 9. Potential energy diagrams and structural configurations for the DFT calculations of conversion of CO_2 to CO*, HCOO, COOH, and HCO on Ru_1/CeO_2. The CO_2 direct dissociation, HCOO formation, and COOH formation mechanisms are depicted by black, orange, and green lines, respectively. The values on the left and right sides of the line represent the activation energies for the forward and backward reactions, respectively. The energy is expressed in eV.

with three lattice O atoms. From this state, the direct dissociation of CO_2 (ΔE_{act} = 0.41 eV, ΔE_R = −1.25 eV) proceeds easier than the formation of HCOO (ΔE_{act} = 3.19 eV, ΔE_R = 0.04 eV) and that of COOH (ΔE_{act} = 1.91 eV, ΔE_R = 0.57 eV).

Starting from the CO*$RuO_2(OH)_2$* state in Figure 9, we explored the direct dissociation of the CO* and H-assisted CO* dissociation pathways. An attempt to move the O atom to the interface between the Ru atom and CeO_2 was unsuccessful, showing that direct dissociation of CO* is not a viable pathway. In our investigation of H-assisted CO* dissociation pathways, we computed an activation energy of 2.12 eV to form HCO* species with a high endothermicity of 1.97 eV. As the reaction energy for the dissociation of HCO* was calculated to be 3.01 eV, it is clear that this pathway is also not viable. Thus, our data show that while CO* formation on the hydrogenated Ru_1/CeO_2 surface involving two OH groups is facile, further dissociation of CO* to form C* precursor species to CH_4 is impossible.

3.3. Microkinetics Simulations. Reaction rates and the product distribution for the CO_2 methanation reaction on the Ru_6/CeO_2 and $Ru_6/RuCe_{x-1}O_{2x-1}$ surfaces were computed by using microkinetics simulations based on DFT-derived reaction energetics. Given the high reaction energy computed for HCO* formation and dissociation on Ru_1/CeO_2, we did not investigate the other elementary reaction steps leading to the formation of CH_4 on this surface. Therefore, this surface is not included in the microkinetics simulations. The pre-exponential factors for the elementary reaction steps are based on a harmonic frequency analysis of the initial and transition states (Tables S2 and S3). In our modeling approach, each adsorbed intermediate is represented as a

https://doi.org/10.1021/acscatal.3c03742
ACS Catal. 2023, 13, 15230−15247

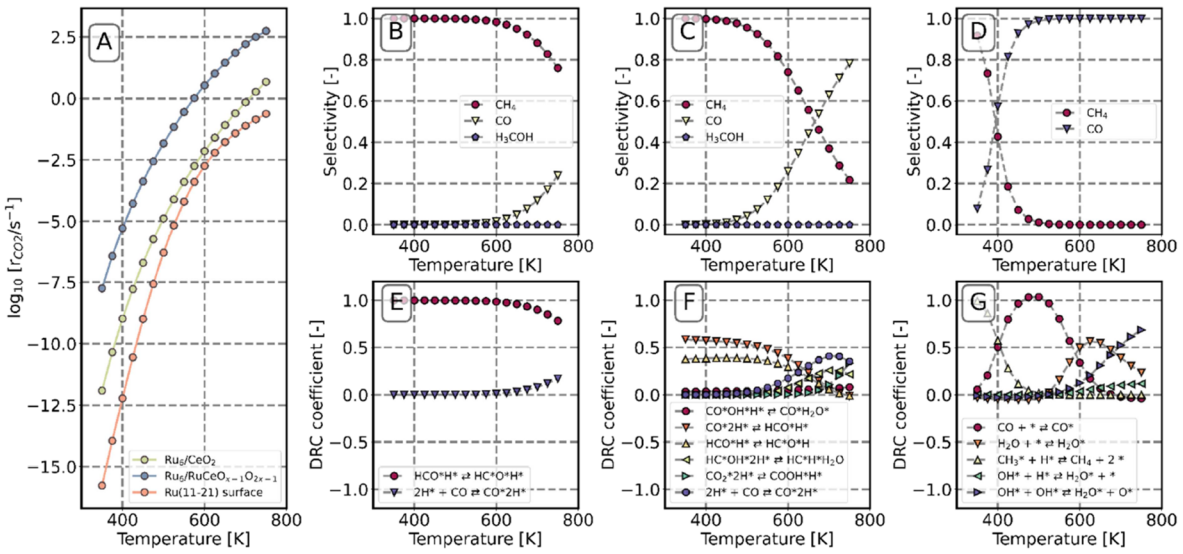

Figure 10. Catalytic performance of Ru_6/CeO_2 (B, E), $Ru_6/RuCe_{x-1}O_{2x-1}$ (C, F), and Ru(11−21) (D, G) as a function of temperature. (A) CO_2 reaction rate; (B−D) distribution of products; (E−G) DRC.

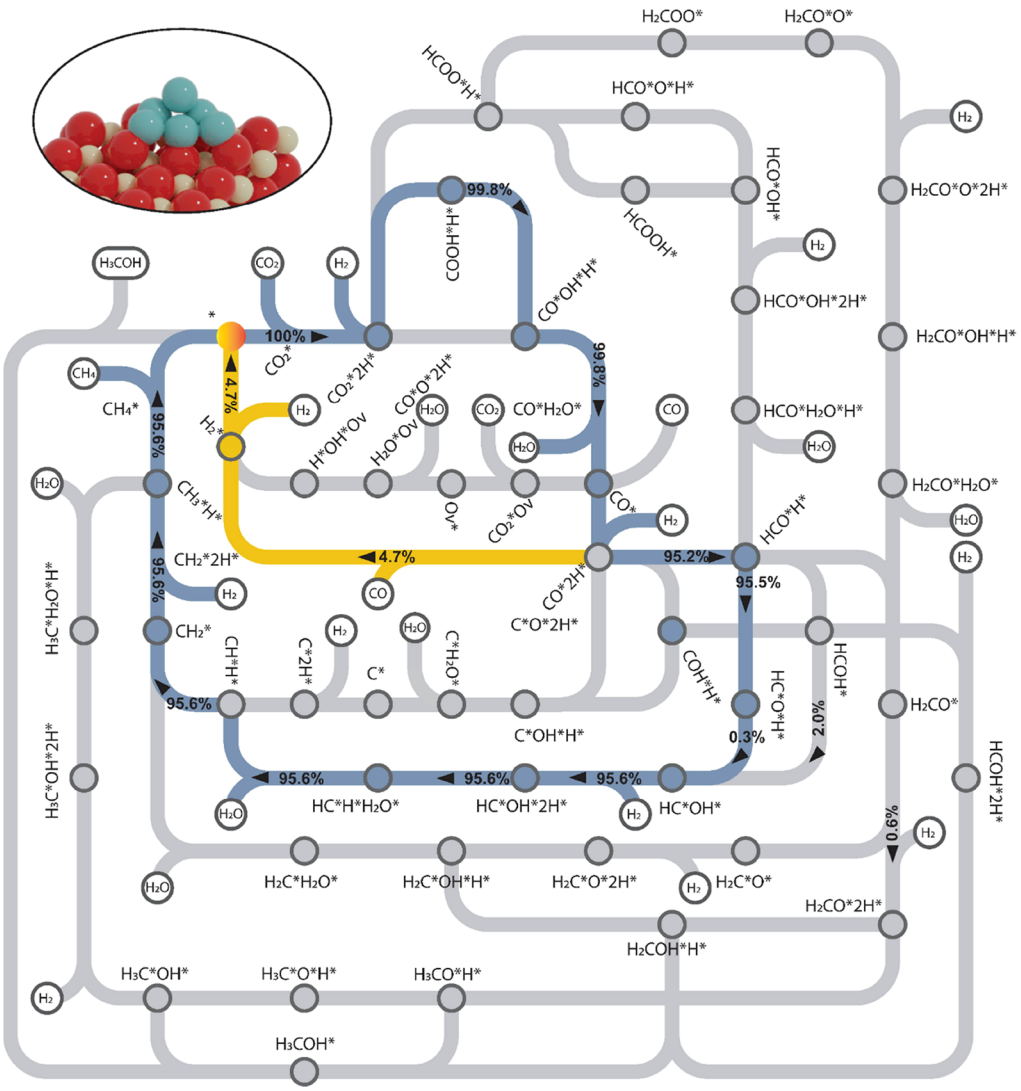

Figure 11. Dominant pathways and normalized fluxes for CO_2 hydrogenation on the Ru_6/CeO_2 surface at 600 K. Pathways for the formation of CO and CH_4 are marked with ochre and blue, respectively.

https://doi.org/10.1021/acscatal.3c03742
ACS Catal. 2023, 13, 15230−15247

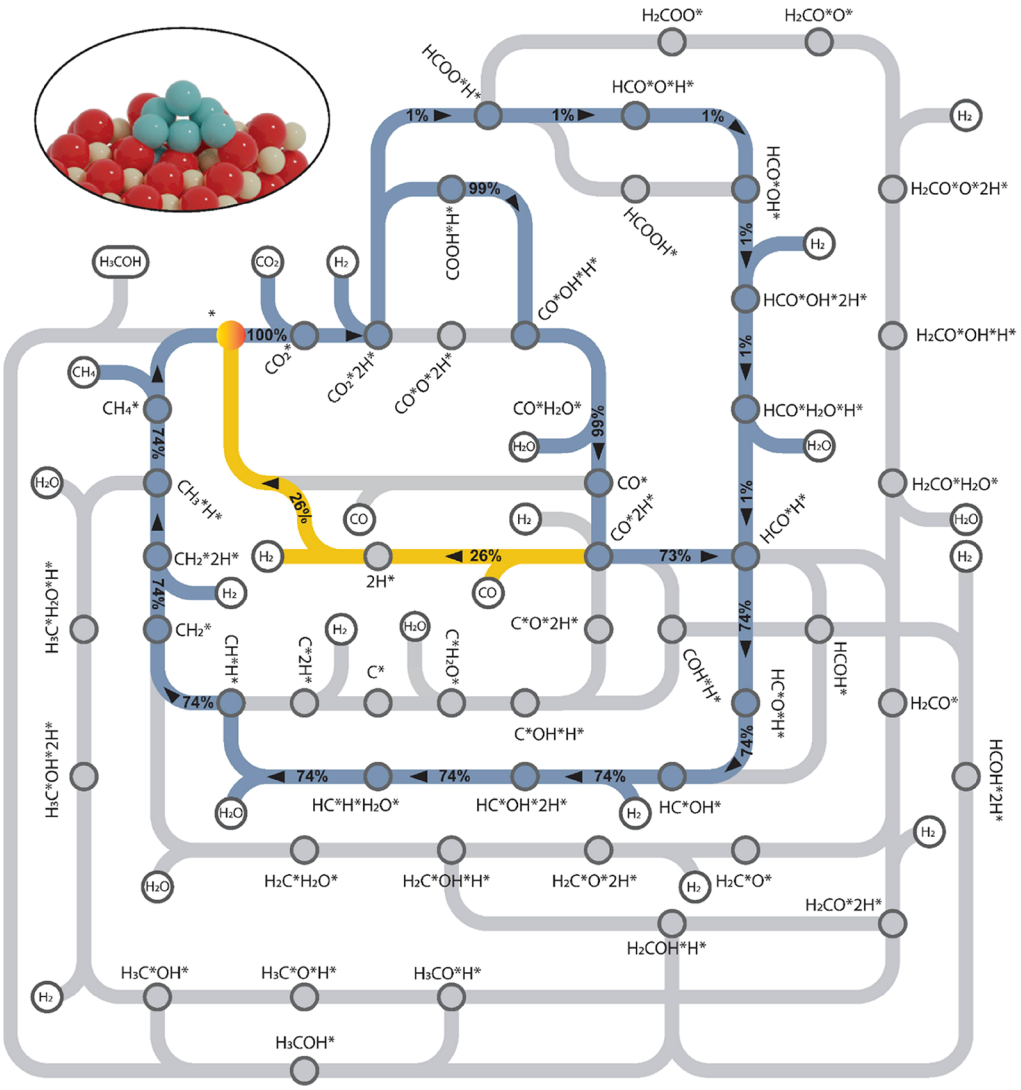

Figure 12. Dominant pathways and normalized fluxes for CO_2 hydrogenation on $Ru_6/RuCe_{x-1}O_{2x-1}$ at 600 K. The CO and CH_4 formation pathways are marked with ochre and blue, respectively.

single active site, resulting in unimolecular elementary reaction steps for all processes, except adsorption and desorption. Microkinetics simulations were conducted in the temperature range of 350−750 K, slightly exceeding the typical temperatures in CO_2 methanation experiments.[18,66,67] The results of the microkinetics simulations are analyzed in terms of reaction pathways contributing to the formation of the various products.

Figure 10 presents the reaction rates (Figure 10A) and product distributions (Figures B and C) for the two models as a function of the temperature. The CO_2 conversion rate over $Ru_6/RuCe_{x-1}O_{2x-1}$ is substantially higher than the rate over Ru_6/CeO_2. At low temperatures, CH_4 is the main product for both surfaces. With increasing temperature, the product distribution shifts to CO. In the whole temperature regime, Ru_6/CeO_2 exhibits a higher selectivity toward CH_4 than $Ru_6/RuCe_{x-1}O_{2x-1}$, which can be attributed to the lower desorption energy of CO on $Ru_6/RuCe_{x-1}O_{2x-1}$ (i.e., 2.26 and 1.89 eV for Ru_6/CeO_2 and $Ru_6/RuCe_{x-1}O_{2x-1}$, respectively). Overall, $Ru_6/RuCe_{x-1}O_{2x-1}$ exhibits a higher CH_4 formation rate than the Ru_6/CeO_2 surface. To explain these observations, the reaction pathways, the DRC, and the degree of selectivity control (DSC) will be discussed.

A so-called reaction pathway analysis was conducted to understand the dominant reaction pathways. Forward and backward reaction rates of all elementary reaction steps are considered and are given as molar fluxes. These fluxes were then normalized to unity so that fractional contributions (F_{norm}) of the different pathways could be discussed. The dominant ways in the reaction pathways, along with the normalized fluxes at a reaction temperature of 600 K for the two surfaces, are highlighted in Figures 11 and 12.

This analysis shows that the dominant pathway for the dissociation of CO_2 involves a COOH* intermediate for both surfaces ($CO_2 \rightarrow COOH^* \rightarrow CO^* + OH^*$). At 600 K, a small amount (4.7%) of the reactant desorbs as CO for Ru_6/CeO_2, while a much larger fraction (26%) desorbs for $Ru_6/RuCeO_{x-1}O_{2x-1}$. This is consistent with the differences of CO desorption energy (i.e., 2.31 eV for Ru_6/CeO_2 vs 1.89 eV for $Ru_6/RuCeO_{x-1}O_{2x-1}$). The rest of the formed CO is hydrogenated to CH_4 via the HCO* species. As the absolute CO_2 reaction rate is higher for $Ru_6/RuCeO_{x-1}O_{2x-1}$, this

https://doi.org/10.1021/acscatal.3c03742
ACS Catal. 2023, 13, 15230−15247

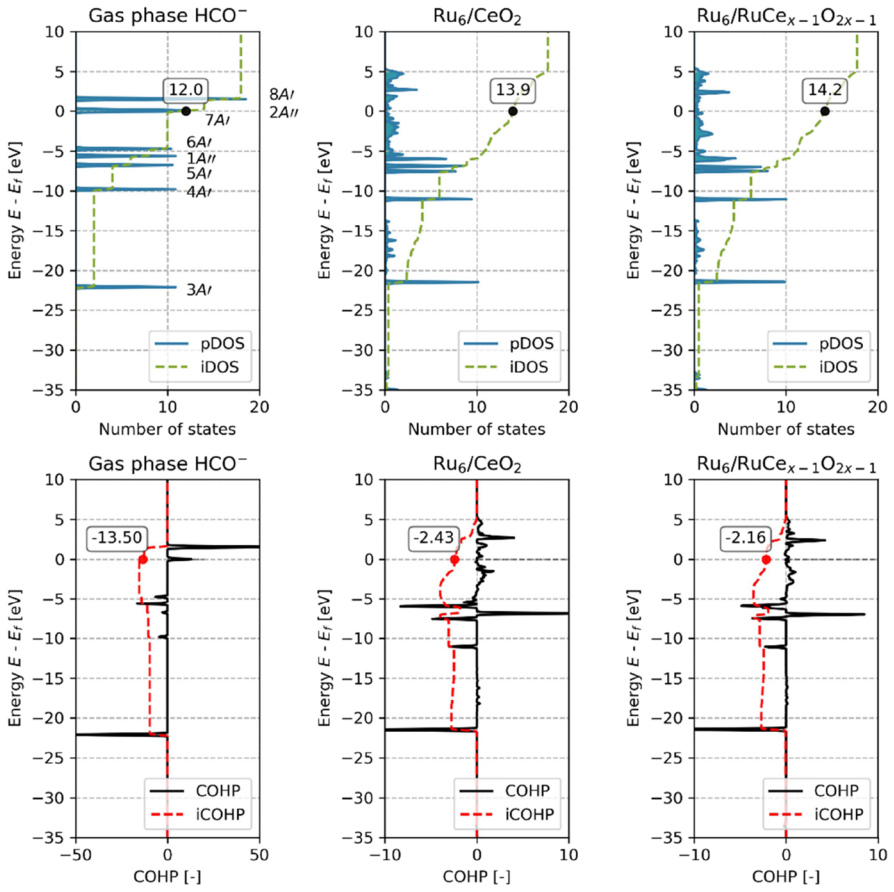

Figure 13. Projected density of states (DOS) and crystal orbital Hamilton population (COHP) analysis of gaseous HCO^- and HCO* adsorbed on Ru_6/CeO_2 and $Ru_6/RuCe_{x-1}O_{2x-1}$. The molecular orbitals (MO) of HCO^- are labeled based on the symmetry groups of the C_s point group. The projected DOS analysis pertains to the H, C, and O atoms. The COHP analysis is conducted for the C−O interactions. The integrated DOS (iDOS) and integrated COHP (iCOHP) under the Fermi level are given in a rounded rectangle above the Fermi energy.

surface also leads to the highest CH_4 reaction rate (cf. Figures S14 and S15).

Degree of Rate Control. To determine which step has the most significant impact on the overall reaction rate, DRC analysis was conducted for CO_2 hydrogenation on Ru_6/CeO_2 and $Ru_6/RuCeO_{x-1}O_{2x-1}$, as shown in Figures 10E and F. For the Ru_6/CeO_2 surface, HCO* dissociation controls the overall reaction rate in the whole temperature regime. Above 600 K, the DRC of the CO desorption step increases, in line with the increased selectivity of CO at higher temperature.

The DRC analysis on the $Ru_6/RuCe_{x-1}O_{2x-1}$ surface shows that the reaction rate is mainly controlled by the formation and dissociation of HCO* at temperatures below 525 K (Figure 10). With an increase in temperature, the DRC of these pathways decreases, while CO desorption starts to control the overall reaction rate. This change goes along with the change in the selectivity from CH_4 to CO. At the high-temperature end, CO_2 hydrogenation to COOH* becomes more rate-controlling.

Degree of Selectivity Control. A DSC analysis was performed to understand which elementary reaction steps control the product distribution. The DSC results for Ru_6/CeO_2 and $Ru_6/RuCe_{x-1}O_{2x-1}$ are displayed in Figures S16 and S17, respectively. For Ru_6/CeO_2, desorption of CO has a negative effect on the CH_4 formation rate, while lowering the activation energy of HCO* dissociation increases the CH_4 formation. This can be explained by considering that CO desorption competes with pathways that lead to C−O dissociation. Lowering the activation energy of HCO* dissociation increases the CH_4 formation. Figure S17 indicates that the selectivity to CH_4 is enhanced by decreasing the activation energy for the formation and dissociation of HCO* and, to a lesser extent, subsequent O* removal. On the other hand, lowering the CO adsorption energy has a negative impact on the CH_4 formation rate. As CH_4 formation directly competes with CO formation, the DSC values for these products show only a change of sign with respect to each other. The positive correlation between CH_4 formation and CO* hydrogenation and its subsequent HCO dissociation is evident. CH_4 formation proceeds predominantly via H-assisted CO* dissociation (Figure 12), and lowering the activation energy involved in this reaction sequence enhances CH_4 selectivity. Conversely, lowering the CO adsorption energy prevents CO* hydrogenation, which leads to a decreased CH_4 selectivity in favor of selectivity to CO.

3.4. Electronic Structure Analysis. The reaction pathway analysis shows that HCO* dissociation to form CH* and O* is a critical step in the reaction network. The lower activation energy (ΔE_{act} = 0.88 eV) for this step on $Ru_6/RuCe_{x-1}O_{2x-1}$ compared to Ru_6/CeO_2 (ΔE_{act} = 1.31 eV) explains the significantly higher rate of CH_4 formation on the doped surface. To understand the difference in the activation energies for HCO* dissociation, a combined partial density of states (pDOS) and crystal orbital Hamilton population (COHP)

https://doi.org/10.1021/acscatal.3c03742
ACS Catal. 2023, 13, 15230−15247

analysis for the C−O bond was performed for both surface models and the anionic gas-phase configuration of HCO^-. The results are shown in Figure 13. HCO^- has 6 occupied valence molecular orbitals (MO). There is a striking similarity between the MO diagrams of CO[68] and HCO^-, wherein the latter can be obtained from the former by splitting each π-state in CO into a lower energy A′ state and a higher energy A″ state, where the A′ and A″ labels correspond to the Mulliken symbols of the symmetry group for the C_s point group.[69] The A″ states are characterized by having a nodal plane as spanned by the H, C, and O atoms. The A′ states lack this nodal feature. An overview of the iso-surfaces of the MOs for HCO^- is provided in Figure S18.

It can be seen from Figure 13 that HCO^- in the gas phase has 12 valence electrons. Upon adsorption on Ru_6/CeO_2 and $Ru_6/RuCe_{x-1}O_{2x-1}$, the 7A′ and 2A″ states shift below the Fermi level and become occupied. This occupancy leads to an increased integrated DOS at the Fermi level, measuring 13.9 and 14.2 for Ru_6/CeO_2 and $Ru_6/RuCe_{x-1}O_{2x-1}$, respectively. The increased DOS for the doped model is consistent with Bader charges (Table S5), which indicates that more electrons are localized at the C atom in HCO* adsorbed on $Ru_6/RuCe_{x-1}O_{2x-1}$. Table S4 reveals a higher electron count within the 3A′, 4A′, 5A′, and 6A′ states of $Ru_6/RuCe_{x-1}O_{2x-1}$ compared to Ru_6/CeO_2. Conversely, fewer electrons are associated with the 1A″ and 7A′+2A″ states in $Ru_6/RuCe_{x-1}O_{2x-1}$. The reduction in electrons for the 1A″ and 7A′+2A″ states fails to compensate for the increase in electrons in the 3A′, 4A′, 5A′, and 6A′ states, resulting in an overall higher electron count on HCO* on $Ru_6/RuCe_{x-1}O_{2x-1}$ compared to HCO* on Ru_6/CeO_2.

The COHP analysis of gaseous HCO^- reveals distinct bonding characteristics among its states. Specifically, the 3A′ MO exhibits strong bonding, while the 4A′, 5A′, 1A″, and 6A′ MOs display only minor bonding characteristics. Additionally, the 7A′ state possesses a little antibonding contribution, while the unoccupied 2A″ state is strongly antibonding.

Upon the adsorption of HCO*, notable changes occur in these states. The 1A″ state transforms from weak bonding to a state with a considerably antibonding nature. Conversely, the 7A′ and 2A″ states maintain their antibonding character, and the 3A′, 4A′, 5A′, and 6A′ states retain their bonding nature. As shown in Table S4, the results allow us to compare the integrated COHP (iCOHP) values between the two surface models. From this table, we can establish that all the bonding states (3A′, 4A′, 5A′, and 6A′) exhibit reduced bonding character. In contrast, the antibonding states (1A″ and 7A′/2A′′) display reduced antibonding character in $Ru_6/RuCe_{x-1}O_{2x-1}$ as compared to Ru_6/CeO_2. Given the negligible differences between the iDOS and iCOHP in the 7A′+2A″ state for Ru_6/CeO_2 and $Ru_6/RuCe_{x-1}O_{2x-1}$, this aspect cannot solely account for the reduced strength of the C−O bond in $Ru_6/RuCe_{x-1}O_{2x-1}$ compared to Ru_6/CeO_2.

The iCOHP values indicate a significant reduction in bonding and antibonding character, with respective values of 0.90 and −0.63 for Ru_6/CeO_2 and $Ru_6/RuCe_{x-1}O_{2x-1}$, respectively. As such, the decreased bonding characteristic of C−O in adsorbed HCO* for the bonding orbitals outweighs the decreased antibonding characteristics in $Ru_6/RuCe_{x-1}O_{2x-1}$. Given the observed persistence of a sharp peak for the 3A′, 4A′, 5A′, and 6A′ states upon adsorption, it can be inferred that these states exhibit a limited tendency to hybridize with the *d*-band on Ru. We thus hypothesize that an increased electron−electron repulsion causes the differences in bonding character due to differences in the Ru−C and Ru−O distances between the two complexes.

To assess this, in Figure S19 the distances of C−Ru, O−Ru, and HC−O bonds for HCO* adsorbed on Ru_6/CeO_2 and $Ru_6/RuCe_{x-1}O_{2x-1}$ are displayed. Since the HCO* complex is adsorbed in different configurations on the two structures, we introduce the following distance metric to describe the Ru−C and Ru−O distances in an averaged sense between the two structures:

$$d = \left(\sum_{i}^{N} |r_{\mathrm{Ru},i\text{-}\mathrm{C/O}}|^{-3} \right)^{-1} \tag{9}$$

This function is constructed to give higher weight to closer distances in the average, compensating for the bias resulting from the difference in the number of Ru atoms in both systems. Although the unit of *d* is Å^3, we use this unit more in the arbitrary sense rather than as a representation of volume. Using this function, the calculated values for the Ru−C distances are $d_{\mathrm{Ru-C}}$= 2.78 Å^3 for Ru_6/CeO_2 and $d_{\mathrm{Ru-C}}$ = 2.79 Å^3 for $Ru_6/RuCe_{x-1}O_{2x-1}$. Similarly, the calculated values for the Ru−O distances are $d_{\mathrm{Ru-O}}$ = 3.93 Å^3 for Ru_6/CeO_2 and $d_{\mathrm{Ru-O}}$ = 3.66 Å^3 for $Ru_6/RuCe_{x-1}O_{2x-1}$. This analysis shows that despite the averaged Ru−C distance being a bit shorter in Ru_6/CeO_2 as compared to $Ru_6/RuCe_{x-1}O_{2x-1}$, it is predominantly the reduced Ru−O distance in the doped model that drives the increased electron−electron repulsion, resulting in a significantly reduced bonding character of the 3A′ state. This rationale is further strengthened by considering the isosurface of the 3A′′′ state, which shows that the majority of the electron density resides on the O atom. Furthermore, it can be observed that the HC−O bond is longer in HCO* adsorbed on $Ru_6/RuCe_{x-1}O_{2x-1}$, which is consistent with the weaker bond strength of HCO.

Consequently, the disparity in bonding characteristics between $Ru_6/RuCe_{x-1}O_{2x-1}$ and Ru_6/CeO_2, where HCO* resides in closer proximity to the Ru atoms on the former system, can be attributed to the stronger electron−electron repulsion of these states with the electron density around the Ru atoms. This result demonstrates that nuanced variations in the coordination of complexes can amplify and generate significant differences in the overall selectivity.

3.5. General Discussion. The results of our first-principles microkinetic simulations will be used to provide further insight into the structure sensitivity of CO_2 methanation on Ru/CeO_2 catalysts. As discussed above, several authors have pointed out the preference for intermediate Ru loading, which presumably can be linked to the presence of small particles, and the role of Ru doping of CeO_2.[4,12,19] A comparison of our CO_2 methanation predictions to those for large nanoparticles can be best made by including microkinetics simulations on a periodic surface that contains sites for CO_2 methanation. For this purpose, we used the DFT energetics of CO methanation on the extended Ru(11−21) surface used earlier in Fischer−Tropsch synthesis,[52] augmented with relevant energetics for CO_2 hydrogenation to CO. The complete reaction energetics are given in Table S6. Figure 10A compares the reaction rate for the Ru(11−21) surface to those of the Ru_6/CeO_2 and $Ru_6/RuCe_{x-1}O_{2x-1}$ surfaces. Under equal reaction conditions, the Ru_6/CeO_2 and $Ru_6/RuCe_{x-1}O_{2x-1}$ models are significantly more active than the extended Ru surface, representing the active sites on nanoparticles large enough not to be perturbed

https://doi.org/10.1021/acscatal.3c03742
ACS Catal. 2023, 13, 15230−15247

by the support. Typical nanoparticles contain a small fraction of step-edge sites, for which Ru(11−21) presents a reasonable surface model needed for CO* dissociation. As such, these results reasonably explain the much lower activity observed for 5 wt % Ru/CeO_2 compared to a 0.5 wt % Ru/CeO_2.[70] As expected, CH_4 is the main product for the Ru(11−21) surface below 400 K, with the CO selectivity increasing at higher temperatures.

While the absolute activity of the various surface models in this study will be affected by the strong binding of CO, we found that the low activity of the Ru(11−21) surface can be attributed to weaker H_2 adsorption in comparison to H_2 adsorption on the cluster models. The adsorption energies of H_2 on Ru_6/CeO_2, $Ru_6/RuCe_{x-1}O_{2x-1}$, and Ru(11−21) surface are −1.15, −0.99, and −0.55 eV, respectively. The CO*2H* state is the most abundant for the Ru_6/CeO_2 and $Ru_6/RuCe_{x-1}O_{2x-1}$ models (Figure S22). To understand this aspect better, we carried out microkinetic simulations for Ru(11−21) with an adjusted H_2 adsorption energy of −0.99 eV corresponding to the H_2 adsorption energy on $Ru_6/RuCe_{x-1}O_{2x-1}$ (Figure S23). The results show that the reaction rate for the extended surface becomes nearly similar to that of the $Ru_6/RuCe_{x-1}O_{2x-1}$ model and CH_4 is the main product in the whole temperature regime. Thus, the higher activity of the Ru_6 clusters as compared to that of Ru nanoparticles is mainly due to stronger H_2 adsorption. Such differences in H_2 adsorption strength have been observed recently for Co,[71] where small Co clusters stabilized by CeO_2 strongly and irreversibly adsorb H_2. In line with our findings, Guo et al. reported that relatively large Ru nanoparticles supported on CeO_2 exhibited a higher reaction order of H_2 in CO_2 methanation than highly dispersed Ru/CeO_2.[12]

While the microkinetics simulations show CH_4 to be the dominant product below 400 K, there is a shift to CO above this temperature, accompanied by a shift of the rate-controlling step to CO desorption. At temperatures above 700 K, the reaction is controlled by H_2O removal, driven by the unfavorable adsorption of H_2 at elevated temperatures. Supporting evidence for this observation can be found in the high surface coverage of the O atoms and the increased reaction order of H_2 (Figure S21).

Self-poisoning by strongly adsorbed reaction intermediates is common in metal nanoparticle catalysis. The relatively low activation energy for CO_2 dissociation on Ru(11−21) (ΔE_{act} = 0.60 eV) results in abundantly adsorbed CO molecules. At low temperatures, there is insufficient thermal energy to overcome the activation energy of C−O dissociation, resulting in a significant accumulation of CO on the surface, as shown in Figure S21A. Combined with the negative reaction order of CO_2 in Figure S21B, we can state that the Ru(11−21) surface is poisoned by adsorbed CO. As already noted in our work on CO hydrogenation on Ru(11−21),[52] we cannot use the CO adsorption energy predicted by DFT due to the overbinding issue.[72] Furthermore, we also considered the effect of lateral interactions. To gauge the impact of overbinding and lateral interactions, we determined how changes in the CO adsorption energy affected the outcomes of the microkinetic simulations for Ru(11−21). Figure S24 shows that lowering the CO adsorption energy corresponds to an increase in the reaction order of CO_2, signifying that reducing the CO adsorption energy mitigates the problem of self-poisoning. Figure S24 also shows that the coverage of empty sites remains relatively low. Lowering the CO adsorption energy improves the selectivity toward CO rather than CH_4. Increasing the temperature would allow for faster CO dissociation, leading to its reaction products remaining on the surface. A further increase in the temperature would benefit from CO desorption over dissociation, as also seen from the selectivity of the reaction as a function of temperature (Figure 10D).

To understand the influence of overbinding of CO on Ru_6/CeO_2 and $Ru_6/RuCe_{x-1}O_{2x-1}$, we conducted microkinetics simulations by decreasing the CO adsorption energy in steps of 0.1 eV to a value of 0.3 eV lower than the original CO adsorption energy. We included Ru(11−21) surface again in these simulations to have a basis of comparison. The results collected in Figures S25−S27 show that these changes in the CO adsorption energy have a minor impact on the CO_2 reaction rate under conditions, where CH_4 is the main reaction product. On the other hand, in a regime where CO is the main product, these changes result in an increase of the CO_2 reaction rate. This leads to a shift in the product distribution for the Ru_6/CeO_2, $Ru_6/RuCe_{x-1}O_{2x-1}$, and Ru(11−21) surface models at low temperatures. Even so, $Ru_6/RuCe_{x-1}O_{2x-1}$ remains the most active surface model for the CO_2 methanation.

As the Ru_6/CeO_2 and $Ru_6/RuCe_{x-1}O_{2x-1}$ models exhibit stronger adsorption of H_2 than the extended Ru(11−21) surface, it is worthwhile to consider the influence of the H coverage. Therefore, we computed activation energies for direct CO* dissociation, HCO* formation, and HCO* dissociation in the presence of an increasing number of H atoms for the two CeO_2-supported Ru models. Table S7 shows that direct CO* dissociation is suppressed when more H atoms are added to the Ru_6 clusters. As expected, these activation energies strongly increase with the addition of more H atoms. Already adding 1 H atom leads to activation energies higher than 2 eV. Although the activation energy for CO* dissociation remains lower for $Ru_6/RuCe_{x-1}O_{2x-1}$ with 1 and 2 H adatoms, it can be stated that high H coverage (3 or 4 H atoms per Ru_6 cluster) will completely suppress direct CO dissociation (i.e., activation energies exceeding 2.5 eV).

Table S8 shows the corresponding data for HCO* formation and HCO* dissociation steps. We find that there is a nearly negligible influence on the reaction energetics, when one more H atom is added to the cluster. Adding more H atoms decreases the activation energies for both HCO* formation and dissociation. It is interesting to note that the addition of 1 or 2 H atoms to Ru_6/CeO_2 does not influence the activation energies of HCO* formation and HCO* dissociation. The effect on the reaction energetics for the $Ru_6/RuCe_{x-1}O_{2x-1}$ surface shows a less clear trend, which appears to be caused by some restructuring of the cluster upon adsorption of H atoms. The most representative results are those that compare 1 and 2 H atoms being added to the surface models, as we found that the free energy of adsorption of H_2 to the Ru_6/CeO_2 is already endergonic at 400 K. Based on the overall activation energies of the two main pathways, we do not expect that the different reaction energetics will significantly affect the qualitative conclusions of our study.

4. CONCLUSIONS

DFT calculations were employed to study the methanation of CO_2 on Ru_1/CeO_2, Ru_6/CeO_2, and $Ru_6/RuCe_{x-1}O_{2x-1}$ surface models as an approach to understanding the structure sensitivity of the Sabatier reaction for Ru/CeO_2 catalysts. A single atom of Ru on CeO_2 can convert CO_2 to CO but lacks

https://doi.org/10.1021/acscatal.3c03742
ACS Catal. 2023, 13, 15230−15247

the active sites for dissociation of the remaining C−O bond. Therefore, this surface model is active only in the reverse water−gas shift reaction. The Ru_6 clusters representing highly dispersed Ru metal phase on stoichiometric and Ru-doped CeO_2 are active methanation catalysts. The main reaction pathway involves the conversion of CO_2 to CO via a carboxyl mechanism. Compared to extended surfaces where direct C−O bond dissociation is facile, CH_x precursors to CH_4 formation are formed by H-assisted C−O bond dissociation via HCO species. The microkinetic simulations predict that the doped model exhibits a higher CO_2 conversion rate. The overall activation energy for HCO dissociation on Ru_6/CeO_2 is higher than the overall activation energy for HCO dissociation on $Ru_6/RuCe_{x-1}O_{2x-1}$. This leads to an overall higher methanation rate for the doped surface. An electronic structure analysis shows that the lower activation energy for HCO dissociation on $Ru_6/RuCe_{x-1}O_{2x-1}$ is due to stronger electron−electron repulsion, which can be attributed to the closer proximity of the reaction intermediate to Ru. The strong H_2 adsorption on small Ru clusters results in higher methanation activity for Ru clusters on CeO_2 compared to a Ru step-edge surface, where the H coverage is low due to stronger competition with adsorbed CO.

■ ASSOCIATED CONTENT

Supporting Information

The Supporting Information is available free of charge at https://pubs.acs.org/doi/10.1021/acscatal.3c03742.

> Supporting methods, configurations of Ru_6/CeO_2 models, relative energies of Ru-for-Ce substitutions in Ru_6/CeO_2, CO_2 adsorption on Ru_6/CeO_2 with an oxygen vacancy, distribution of Ce^{3+}, kinetic parameters used in microkinetics simulations, configurations of intermediates in the reaction networks, fluxes analysis, DSC analysis, electronic structure analysis, CO_2 methanation mechanism on Ru(11−21) surface, the effect of CO overbinding and the effect of H coverage on CO direct dissociation and HCO formation and dissociation (PDF)

■ AUTHOR INFORMATION

Corresponding Author

Emiel J. M. Hensen − *Laboratory of Inorganic Materials and Catalysis, Department of Chemical Engineering and Chemistry, Eindhoven University of Technology, 5600 MB Eindhoven, the Netherlands;* orcid.org/0000-0002-9754-2417; Email: e.j.m.hensen@tue.nl

Authors

Lulu Chen − *Laboratory of Inorganic Materials and Catalysis, Department of Chemical Engineering and Chemistry, Eindhoven University of Technology, 5600 MB Eindhoven, the Netherlands*

Ivo A. W. Filot − *Laboratory of Inorganic Materials and Catalysis, Department of Chemical Engineering and Chemistry, Eindhoven University of Technology, 5600 MB Eindhoven, the Netherlands;* orcid.org/0000-0003-1403-8379

Complete contact information is available at: https://pubs.acs.org/10.1021/acscatal.3c03742

Notes

The authors declare no competing financial interest.

■ ACKNOWLEDGMENTS

We acknowledge the financial support granted by the China Scholarship Council. The authors acknowledge NWO and SurfSARA for providing computational resources to carry out the DFT calculations.

■ REFERENCES

(1) Roy, S.; Cherevotan, A.; Peter, S. C. Thermochemical CO_2 Hydrogenation to Single Carbon Products: Scientific and Technological Challenges. *ACS Energy Lett.* **2018**, *3*, 1938−1966.

(2) Jomjaree, T.; Sintuya, P.; Srifa, A.; Koo-amornpattana, W.; Kiatphuengporn, S.; Assabumrungrat, S.; Sudoh, M.; Watanabe, R.; Fukuhara, C.; Ratchahat, S. Catalytic Performance of Ni Catalysts Supported on CeO_2 with Different Morphologies for Low-Temperature CO_2 Methanation. *Catal. Today* **2021**, *375*, 234−244.

(3) Tada, S.; Shimizu, T.; Kameyama, H.; Haneda, T.; Kikuchi, R. Ni/CeO_2 Catalysts with High CO_2 Methanation Activity and High CH_4 Selectivity at Low Temperatures. *Int. J. Hydrogen Energy* **2012**, *37*, 5527−5531.

(4) López-Rodríguez, S.; Davó-Quiñonero, A.; Bailón-García, E.; Lozano-Castelló, D.; Bueno-López, A. Effect of Ru Loading on Ru/CeO_2 Catalysts for CO_2 Methanation. *Mol. Catal.* **2021**, *515*, No. 111911.

(5) Wang, F.; Li, C.; Zhang, X.; Wei, M.; Evans, D. G.; Duan, X. Catalytic Behavior of Supported Ru Nanoparticles on the {1 0 0}, {1 1 0}, and {1 1 1} Facet of CeO_2. *J. Catal.* **2015**, *329* (1), 177−186.

(6) Rui, N.; Zhang, X.; Zhang, F.; Liu, Z.; Cao, X.; Xie, Z.; Zou, R.; Senanayake, S. D.; Yang, Y.; Rodriguez, J. A.; Liu, C. J. Highly Active Ni/CeO_2 Catalyst for CO_2 Methanation: Preparation and Characterization. *Appl. Catal., B* **2021**, *282*, No. 119581.

(7) Yang, Y.; Liu, J.; Liu, F.; Wu, D. Reaction Mechanism of CO_2 Methanation over Rh/TiO_2 Catalyst. *Fuel* **2020**, *276*, No. 118093.

(8) Vrijburg, W. L.; Garbarino, G.; Chen, W.; Parastaev, A.; Longo, A.; Pidko, E. A.; Hensen, E. J. M. Ni-Mn Catalysts on Silica-Modified Alumina for CO_2 Methanation. *J. Catal.* **2020**, *382*, 358−371.

(9) Bian, Z.; Chan, Y. M.; Yu, Y.; Kawi, S. Morphology Dependence of Catalytic Properties of Ni/CeO_2 for CO_2 Methanation: A Kinetic and Mechanism Study. *Catal. Today* **2020**, *347*, 31−38.

(10) Dreyer, J. A. H.; Li, P.; Zhang, L.; Beh, G. K.; Zhang, R.; Sit, P. H. L.; Teoh, W. Y. Influence of the Oxide Support Reducibility on the CO_2 Methanation over Ru-Based Catalysts. *Appl. Catal., B* **2017**, *219*, 715−726.

(11) Quindimil, A.; De-La-Torre, U.; Pereda-Ayo, B.; Davó-Quiñonero, A.; Bailón-García, E.; Lozano-Castelló, D.; González-Marcos, J. A.; Bueno-López, A.; González-Velasco, J. R. Effect of Metal Loading on the CO_2 Methanation: A Comparison between Alumina Supported Ni and Ru Catalysts. *Catal. Today* **2020**, *356*, 419−432.

(12) Guo, Y.; Mei, S.; Yuan, K.; Wang, D. J.; Liu, H. C.; Yan, C. H.; Zhang, Y. W. Low-Temperature CO_2 Methanation over CeO_2-Supported Ru Single Atoms, Nanoclusters, and Nanoparticles Competitively Tuned by Strong Metal-Support Interactions and H-Spillover Effect. *ACS Catal.* **2018**, *8* (7), 6203−6215.

(13) Vrijburg, W. L.; Moioli, E.; Chen, W.; Zhang, M.; Terlingen, B. J. P.; Zijlstra, B.; Filot, I. A. W.; Züttel, A.; Pidko, E. A.; Hensen, E. J. M. Efficient Base-Metal $NiMn/TiO_2$ Catalyst for CO_2 Methanation. *ACS Catal.* **2019**, *9* (9), 7823−7839.

(14) Aitbekova, A.; Wu, L.; Wrasman, C. J.; Boubnov, A.; Hoffman, A. S.; Goodman, E. D.; Bare, S. R.; Cargnello, M. Low-Temperature Restructuring of CeO_2-Supported Ru Nanoparticles Determines Selectivity in CO_2 Catalytic Reduction. *J. Am. Chem. Soc.* **2018**, *140* (42), 13736−13745.

(15) Kwak, J. H.; Kovarik, L.; Szanyi, J. CO_2 Reduction on Supported Ru/Al_2O_3 Catalysts: Cluster Size Dependence of Product Selectivity. *ACS Catal.* **2013**, *3* (11), 2449−2455.

(16) Mansour, H.; Iglesia, E. Mechanistic Connections between CO_2 and CO Hydrogenation on Dispersed Ruthenium Nanoparticles. *J. Am. Chem. Soc.* **2021**, *143*, 11582−11594.
(17) Sun, S.; Sun, H.; Guan, S.; Xu, S.; Wu, C. Integrated CO_2 Capture and Methanation on Ru/CeO_2-MgO Combined Materials: Morphology Effect from CeO_2 Support *Fuel* **2022**, *317*, 123420, .
(18) Wang, F.; He, S.; Chen, H.; Wang, B.; Zheng, L.; Wei, M.; Evans, D. G.; Duan, X. Active Site Dependent Reaction Mechanism over Ru/CeO_2 Catalyst toward CO_2 Methanation. *J. Am. Chem. Soc.* **2016**, *138* (19), 6298−6305.
(19) Wang, C.; Sun, H.; Liu, X.; Jin, X.; Feng, Y.; Shi, H.; Wang, D.; Zhang, Y.; Wang, Y.; Yan, Z. Low-Temperature CO_2 Methanation over Ru/CeO_2: Investigation into Ru Loadings. *Fuel* **2023**, *345*, No. 128238.
(20) Pereira-Hernández, X. I.; DeLaRiva, A.; Muravev, V.; Kunwar, D.; Xiong, H.; Sudduth, B.; Engelhard, M.; Kovarik, L.; Hensen, E. J. M.; Wang, Y.; Datye, A. K. Tuning Pt-CeO_2 Interactions by High-Temperature Vapor-Phase Synthesis for Improved Reducibility of Lattice Oxygen. *Nat. Commun.* **2019**, *10*, 1358.
(21) Zhang, L.; Spezzati, G.; Muravev, V.; Verheijen, M. A.; Zijlstra, B.; Filot, I. A. W.; Su, Y. Q.; Chang, M. W.; Hensen, E. J. M. Improved Pd/CeO_2 catalysts for Low-Temperature NO Reduction: Activation of CeO_2 lattice Oxygen by Fe Doping. *ACS Catal.* **2021**, *11*, 5614−5627.
(22) Su, Y. Q.; Zhang, L.; Muravev, V.; Hensen, E. J. M. Lattice Oxygen Activation in Transition Metal Doped Ceria. *Chin. J. Catal.* **2020**, *41*, 977−984.
(23) Xu, X.; Liu, L.; Tong, Y.; Fang, X.; Xu, J.; Jiang, D. E.; Wang, X. Facile Cr^{3+}-Doping Strategy Dramatically Promoting Ru/CeO_2 for Low-Temperature CO_2 Methanation: Unraveling the Roles of Surface Oxygen Vacancies and Hydroxyl Groups. *ACS Catal.* **2021**, *11*, 5762−5775.
(24) López-Rodríguez, S.; Davó-Quiñonero, A.; Bailón-García, E.; Lozano-Castelló, D.; Herrera, F. C.; Pellegrin, E.; Escudero, C.; García-Melchor, M.; Bueno-López, A. Elucidating the Role of the Metal Catalyst and Oxide Support in the Ru/CeO_2-Catalyzed CO_2 Methanation Mechanism. *J. Phys. Chem. C* **2021**, *125* (46), 25533−25544.
(25) Ma, S.; Song, W.; Liu, B.; Zheng, H.; Deng, J.; Zhong, W.; Liu, J.; Gong, X. Q.; Zhao, Z. Elucidation of the High CO2 Reduction Selectivity of Isolated Rh Supported on TiO_2: A DFT Study. *Catal. Sci. Technol.* **2016**, *6* (15), 6128−6136.
(26) Kresse, G.; Furthmüller, J. Efficiency of Ab-Initio Total Energy Calculations for Metals and Semiconductors Using a Plane-Wave Basis Set. *Comput. Mater. Sci.* **1996**, *6*, 15−50.
(27) Kresse, G.; Furthmüller, J. Efficient Iterative Schemes for Ab Initio Total-Energy Calculations Using a Plane-Wave Basis Set. *Phys. Rev. B: Condens. Matter Mater. Phys.* **1996**, *54*, 11169.
(28) Kresse, G.; Hafner, J. Ab Initio Molecular Dynamics for Liquid Metals. *Phys. Rev. B* **1993**, *47*, 558−561.
(29) Perdew, J. P.; Burke, K.; Ernzerhof, M. Generalized Gradient Approximation Made Simple. *Phys. Rev. Lett.* **1996**, *77*, 3865−3868.
(30) Blöchl, P. E. Projector Augmented-Wave Method. *Phys. Rev. B* **1994**, *50*, 17953−17979.
(31) Joubert, D. From Ultrasoft Pseudopotentials to the Projector Augmented-Wave Method. *Phys. Rev. B: Condens. Matter Mater. Phys.* **1999**, *59*, 1758−1775.
(32) Fry, P. W.; Itskevich, I. E.; Parnell, S. R.; Finley, J. J.; Wilson, L. R.; Schumacher, K. L.; Mowbray, D. J.; Skolnick, M. S.; Cullis, A. G.; Hopkinson, M.; Clark, J. C.; Hill, G. *Phys. Rev. B* **2000**, *62*, 784−791.
(33) Dudarev, S. L.; Botton, G. A.; Savrasov, S. Y.; Humphreys, C. J.; Sutton, A. P. Electron-Energy-Loss Spectra and the Structural Stability of Nickel Oxide: An LSDA+U Study. *Phys. Rev. B* **1998**, *57*, 1505.
(34) Košmider, K.; Brázdová, V.; Ganduglia-Pirovano, M. V.; Pérez, R. Do Au Atoms Titrate Ce^{3+} Ions at the CeO_{2-x}(111) Surface? *J. Phys. Chem. C* **2016**, *120*, 927−933.
(35) Fabris, S.; Vicario, G.; Balducci, G.; de Gironcoli, S.; Baroni, S. Electronic and Atomistic Structures of Clean and Reduced Ceria Surfaces. *J. Phys. Chem. B* **2005**, *109*, 22860−22867.
(36) Chen, Y.; Hu, P.; Lee, M. H.; Wang, H. Au on (1 1 1) and (1 1 0) Surfaces of CeO_2: A Density-Functional Theory Study. *Surf. Sci.* **2008**, *602*, 1736−1741.
(37) Zhang, C.; Michaelides, A.; Jenkins, S. J. Theory of Gold on Ceria. *Phys. Chem. Chem. Phys.* **2011**, *13*, 22−33.
(38) Camellone, M. F.; Fabris, S. Reaction Mechanisms for the CO Oxidation on Au/CeO_2 Catalysts: Activity of Substitutional Au^{3+}/Au^{+} Cations and Deactivation of Supported Au^{+} Adatoms. *J. Am. Chem. Soc.* **2009**, *131*, 10473−10483.
(39) Grimme, S.; Antony, J.; Ehrlich, S.; Krieg, H. A Consistent and Accurate Ab Initio Parametrization of Density Functional Dispersion Correction (DFT-D) for the 94 Elements H-Pu. *J. Chem. Phys.* **2010**, *132*, 154104.
(40) Grimme, S.; Ehrlich, S.; Goerigk, L. Effect of the Damping Function in Dispersion Corrected Density Functional Theory. *J. Comput. Chem.* **2011**, *32*, 1456−1465.
(41) Henkelman, G.; Uberuaga, B. P.; Jónsson, H. Climbing Image Nudged Elastic Band Method for Finding Saddle Points and Minimum Energy Paths. *J. Chem. Phys.* **2000**, *113*, 9901−9904.
(42) Maintz, S.; Deringer, V. L.; Tchougréeff, A. L.; Dronskowski, R. LOBSTER: A Tool to Extract Chemical Bonding from Plane-Wave Based DFT. *J. Comput. Chem.* **2016**, *37*, 1030−1035.
(43) Deringer, V. L.; Tchougréeff, A. L.; Dronskowski, R. Crystal Orbital Hamilton Population (COHP) Analysis as Projected from Plane-Wave Basis Sets. *J. Phys. Chem. A* **2011**, *115*, 5461−5466.
(44) Henkelman, G.; Arnaldsson, A.; Jónsson, H. A Fast and Robust Algorithm for Bader Decomposition of Charge Density. *Comput. Mater. Sci.* **2006**, *36*, 354−360.
(45) Gerward, L.; Olsen, J. S. Powder Diffraction Analysis of Cerium Dioxide at High Pressure. *Powder Diffr.* **1993**, *8*, 127−129.
(46) Nolan, M.; Parker, S. C.; Watson, G. W. The Electronic Structure of Oxygen Vacancy Defects at the Low Index Surfaces of Ceria. *Surf. Sci.* **2005**, *595*, 223−232.
(47) Paier, J.; Penschke, C.; Sauer, J. Oxygen Defects and Surface Chemistry of Ceria: Quantum Chemical Studies Compared to Experiment. *Chem. Rev.* **2013**, *113*, 3949−3985.
(48) Ganduglia-Pirovano, M. V.; Hofmann, A.; Sauer, J. Oxygen Vacancies in Transition Metal and Rare Earth Oxides: Current State of Understanding and Remaining Challenges. *Surf. Sci. Rep.* **2007**, *62*, 219−270.
(49) Mullins, D. R. The Surface Chemistry of Cerium Oxide. *Surf. Sci. Rep.* **2015**, *70*, 42−85.
(50) Fronzi, M.; Soon, A.; Delley, B.; Traversa, E.; Stampfl, C. Stability and Morphology of Cerium Oxide Surfaces in an Oxidizing Environment: A First-Principles Investigation. *J. Chem. Phys.* **2009**, *131*, 104701.
(51) Nitoń, P.; Zywociński, A.; Fiałkowski, M.; Hołyst, R. A "Nano-Windmill" Driven by a Flux of Water Vapour: A Comparison to the Rotating ATPase. *Nanoscale* **2013**, *5*, 9732−9738.
(52) Filot, I. A. W.; Van Santen, R. A.; Hensen, E. J. M. The Optimally Performing Fischer−Tropsch Catalyst. *Angew. Chem., Int. Ed.* **2014**, *53*, 12746−12750.
(53) Campbell, C. T. Future Directions and Industrial Perspectives Micro- and Macro-Kinetics: Their Relationship in Heterogeneous Catalysis. *Top. Catal.* **1994**, *1*, 353−366.
(54) Manz, T. A.; Limas, N. G. Introducing DDEC6 Atomic Population Analysis: Part 1. Charge Partitioning Theory and Methodology. *RSC Adv.* **2016**, *6*, 47771−47801.
(55) Kehoe, A. B.; Scanlon, D. O.; Watson, G. W. Role of Lattice Distortions in the Oxygen Storage Capacity of Divalently Doped CeO_2. *Chem. Mater.* **2011**, *23*, 4464−4468.
(56) Qu, P. F.; Wang, G. C. Theoretical Insight into the Strong Size-Dependence of Dry Reforming of Methane over Ru/CeO_2. *J. CO2 Util.* **2022**, *65*, No. 102221.
(57) Li, F.; Li, L.; Liu, X.; Zeng, X. C.; Chen, Z. High-Performance Ru_1/CeO_2 Single-Atom Catalyst for CO Oxidation: A Computational Exploration. *ChemPhysChem* **2016**, *17*, 3170−3175.

https://doi.org/10.1021/acscatal.3c03742
ACS Catal. 2023, 13, 15230−15247

(58) Chen, H. T. First-Principles Study of CO Adsorption and Oxidation on Ru-Doped CeO_2(111) Surface. *J. Phys. Chem. C* **2012**, *116*, 6239−6246.
(59) Hahn, K. R.; Seitsonen, A. P.; Iannuzzi, M.; Hutter, J. Functionalization of CeO_2(111) by Deposition of Small Ni Clusters: Effects on CO_2 Adsorption and O Vacancy Formation. *ChemCatChem* **2015**, *7*, 625−634.
(60) Qu, P. F.; Wang, G. C. DFT-Based Microkinetic Model Analysis of Dry Reforming of Methane over Ru_7/CeO_2(111) and Ru_7/CeO_2(110): Key Role of Surface Lattice Oxygen Vacancy. *Catal. Sci. Technol.* **2022**, *12*, 1880−1891.
(61) Gahleitner, G. Hydrogen from Renewable Electricity: An International Review of Power-to-Gas Pilot Plants for Stationary Applications. *Int. J. Hydrogen Energy* **2013**, *38*, 2039−2061.
(62) Shetty, S.; Jansen, A. P. J.; Van Santen, R. A. Direct versus Hydrogen-Assisted CO Dissociation. *J. Am. Chem. Soc.* **2009**, *131*, 12874−12875.
(63) Alfonso, D. R. Further Theoretical Evidence for Hydrogen-Assisted CO Dissociation on Ru(0001). *J. Phys. Chem. C* **2013**, *117*, 20562−20571.
(64) Chang, M. W.; Zhang, L.; Davids, M.; Filot, I. A. W.; Hensen, E. J. M. Dynamics of Gold Clusters on Ceria during CO Oxidation *J. Catal.* **2020**, *392*, 39, DOI: 10.1016/j.jcat.2020.09.027.
(65) Liu, J. X.; Su, Y.; Filot, I. A. W.; Hensen, E. J. M. A Linear Scaling Relation for CO Oxidation on CeO_2-Supported Pd. *J. Am. Chem. Soc.* **2018**, *140*, 4580−4587.
(66) Lustemberg, P. G.; Mao, Z.; Salcedo, A.; Irigoyen, B.; Ganduglia-Pirovano, M. V.; Campbell, C. T. Nature of the Active Sites on Ni/CeO_2 Catalysts for Methane Conversions. *ACS Catal.* **2021**, *11*, 10604−10613.
(67) Aziz, M. A. A.; Jalil, A. A.; Triwahyono, S.; Mukti, R. R.; Taufiq-Yap, Y. H.; Sazegar, M. R. Highly Active Ni-Promoted Mesostructured Silica Nanoparticles for CO_2 Methanation. *Appl. Catal., B* **2014**, *147*, 359−368.
(68) Jorgensen, W. L.; Salem, L. *The Organic Chemist's Book of Orbitals*; A Subsidiary of Harcourt Brace Jovanovich: New York, 1973.
(69) Bishop, D. M.; Klein, D. J. *Group Theory and Chemistry*; Dover Publication Inc., 1975.
(70) Sharma, S.; Hu, Z.; Zhang, P.; McFarland, E. W.; Metiu, H. CO_2 Methanation on Ru-Doped Ceria. *J. Catal.* **2011**, *278*, 297−309.
(71) Parastaev, A.; Muravev, V.; Osta, E. H.; Kimpel, T. F.; Simons, J. F. M.; van Hoof, A. J. F.; Uslamin, E.; Zhang, L.; Struijs, J. J. C.; Burueva, D. B.; Pokochueva, E. V.; Kovtunov, K. V.; Koptyug, I. V.; Villar-Garcia, I. J.; Escudero, C.; Altantzis, T.; Liu, P.; Béché, A.; Bals, S.; Kosinov, N.; Hensen, E. J. M. Breaking Structure Sensitivity in CO_2 Hydrogenation by Tuning Metal−Oxide Interfaces in Supported Cobalt Nanoparticles. *Nat. Catal.* **2022**, *5*, 1051−1060.
(72) Abild-Pedersen, F.; Andersson, M. P. CO Adsorption Energies on Metals with Correction for High Coordination Adsorption Sites - A Density Functional Study. *Surf. Sci.* **2007**, *601*, 1747−1753.

https://doi.org/10.1021/acscatal.3c03742
ACS Catal. 2023, 13, 15230−15247